CANCER

G6PD-mediated increase in de novo NADP$^+$ biosynthesis promotes antioxidant defense and tumor metastasis

Yang Zhang[1,2], Yi Xu[1,2], Wenyun Lu[3,4], Jinyang Li[2,5,6], Sixiang Yu[1], Eric J. Brown[1,2], Ben Z. Stanger[2,5,6], Joshua D. Rabinowitz[3,4], Xiaolu Yang[1,2]*

Metastasizing cancer cells are able to withstand high levels of oxidative stress through mechanisms that are poorly understood. Here, we show that under various oxidative stress conditions, pancreatic cancer cells markedly expand NADPH and NADP$^+$ pools. This expansion is due to up-regulation of glucose-6-phosphate dehydrogenase (G6PD), which stimulates the cytoplasmic nicotinamide adenine dinucleotide kinase (NADK1) to produce NADP$^+$ while converting NADP$^+$ to NADPH. G6PD is activated by the transcription factor TAp73, which is, in turn, regulated by two pathways. Nuclear factor–erythroid 2 p45-related factor-2 suppresses expression of the ubiquitin ligase PIRH2, stabilizing the TAp73 protein. Checkpoint kinases 1/2 and E2F1 induce expression of the *TAp73* gene. Levels of G6PD and its upstream activators are elevated in metastatic pancreatic cancer. Knocking down G6PD impedes pancreatic cancer metastasis, whereas forced G6PD expression promotes it. These findings reveal an intracellular network that maintains redox homeostasis through G6PD-mediated increase in de novo NADP$^+$ biosynthesis, which may be co-opted by tumor cells to enable metastasis.

INTRODUCTION

Reactive oxygen species (ROS), which are generated constantly in the cell as part of aerobic life, play an important role in physiological processes when present at relatively low levels (*1*, *2*). High levels of ROS, however, can damage essential cellular components, including DNA, protein, and lipid. Therefore, maintaining redox homeostasis is crucial for cell survival and function (*3*). Accumulating evidence indicates that tumor cells experience overproduction of ROS due to intrinsic and extrinsic factors (*4*–*6*). Notable among them is the loss of extracellular matrix attachment during excessive proliferation at the primary tumor site and especially during the multistep process of metastasis including migration, local invasion, entry into the circulation, extravasation, and colonization of distant organs (*7*, *8*). Exogenous antioxidants can promote tumor initiation and metastasis (*9*–*14*), underscoring the importance of ROS reduction for tumor cells.

Normal and malignant cells depend on various defense systems to keep ROS levels below the lethal threshold (*7*, *15*–*17*). These systems, including the abundant glutathione and peroxiredoxin systems, are, in turn, maintained by the reduced form of NADP$^+$ [nicotinamide (NAM) adenine dinucleotide (NAD$^+$) phosphate] (NADPH), a universal reducing equivalent (*6*, *18*). Cellular NADPH levels are primarily determined by two processes: regeneration from NADP$^+$ and de novo NADP$^+$ synthesis (*19*, *20*). A number of metabolic pathways can regenerate NADPH from NADP$^+$ (*21*–*23*). Among them, the oxidative pentose phosphate pathway (PPP), with glucose-6-phosphate dehydrogenase (G6PD) as its rate-limiting enzyme, not only produces most of the NADPH in a variety of cells (*24*, *25*) but also responds to oxidative stresses through both short- and long-term mechanisms. Short-term mechanisms include allosteric regulation and posttranslational modifications that either directly increase G6PD activity or inhibit glycolytic enzymes to redirect glycolytic intermediates to the PPP (*26*–*30*). These acute responses are often followed by a long-term increase in the expression of the *G6PD* gene. However, both causes and consequences of increased *G6PD* expression are not well understood.

In response to oxidative stress, nuclear factor–erythroid 2 p45-related factor-2 (NRF2), a master regulator of cellular redox response (*31*), stimulates the expression of a wide range of antioxidant and detoxification genes, including *G6PD* (*32*). However, it is not known whether NRF2 directly activates the *G6PD* gene or to what extent G6PD contributes to NRF2-directed antioxidant defense. Under normal circumstances, G6PD operates at a very low level compared to its maximal capacity (e.g., 1 to 2%) (*33*, *34*). Thus, in principle, the metabolic flux through G6PD can be vastly accentuated without the need of higher G6PD expression. This raises an interesting possibility that G6PD up-regulation might have important consequences beyond NADPH regeneration.

Cells normally maintain a high NADPH/NADP$^+$ ratio, in favor of the reduced form (*19*). As a consequence, a substantial increase in NADPH levels would depend on de novo synthesis of NADP$^+$ (*19*, *20*), which is catalyzed by NAD$^+$ kinase (NADK) (*19*, *20*). NADK exists as a cytoplasmic (NADK1) and a mitochondrial (NADK2) isoform. NADK1 can be activated by AKT- and protein kinase C (PKC)–mediated phosphorylation in a cell context-dependent manner (*35*, *36*), which links NADK1 to mitogenic signaling. However, the function and regulation of NADK under oxidative stress conditions remain undefined.

Pancreatic cancer is a highly lethal form of cancer with a 5-year survival rate of only ~10%. At the time of the diagnosis, nearly 50% of patients already present with distant metastases (*37*, *38*). As ROS may represent a key barrier for metastasis (*10*), we examine how pancreatic cancer cells may withstand high redox stress. We find that

[1]Department of Cancer Biology, University of Pennsylvania, Philadelphia, PA 19104, USA. [2]Abramson Family Cancer Research Institute, University of Pennsylvania, Philadelphia, PA 19104, USA. [3]Lewis-Sigler Institute for Integrative Genomics, Princeton University, Princeton, NJ 08540, USA. [4]Department of Chemistry, Princeton University, Princeton, NJ 08540, USA. [5]Department of Medicine, University of Pennsylvania, Philadelphia, PA 19104, USA. [6]Department of Cell and Developmental Biology, University of Pennsylvania, Philadelphia, PA 19104, USA.
*Corresponding author. Email: xyang@pennmedicine.upenn.edu

pancreatic cancer cells markedly expand the NADPH and $NADP^+$ pools under various oxidative stress conditions. This expansion is due to increased metabolic flux through NADK1. NADK1 protein levels remain unchanged; instead, G6PD, which can bind to and stimulate the activity of NADK1 (*14*), is up-regulated by redox stress. We identify the transactivation (TA) isoform of p73, a structural homolog of the tumor suppressor p53, as the redox-responsive, proximal transcriptional factor of *G6PD*. We further define two pathways that activate TAp73 via distinct mechanisms. One pathway involves NRF2, which directly suppresses the expression of the ubiquitin ligase PIRH2, stabilizing the TAp73 protein. The other involves DNA damage checkpoint kinases CHK1/2 and the transcription factor E2F1, which become activated following oxidative stress to induce the expression of the *TAp73* gene. These results reveal a cellular redox homeostasis mechanism that, in response to redox imbalance, activates de novo $NADP^+$ synthesis via the up-regulation of G6PD to bolster the capacity of antioxidant systems. The importance of this network in tumorigenesis is underscored by the role of NADK1, G6PD, and other components in the growth and metastasis of pancreatic cancer.

RESULTS

Expansion of NADPH and $NADP^+$ pools under oxidative stress conditions

Tumor initiation and metastasis involve the detachment of cancer cells from their natural extracellular matrix, a process that elicits strong oxidative stress (*7*). To investigate how cancer cells may respond to this oxidative stress, we examined NADPH and $NADP^+$ levels in pancreatic cancer PANC-1 cells following matrix detachment. As expected, matrix-detached PANC-1 cells showed higher ROS levels (Fig. 1, A and B) and a lower NADPH/$NADP^+$ ratio (Fig. 1C) compared to matrix-attached cells. However, the NADPH pool was also expanded in PANC-1 cells following matrix detachment, reaching a ~60% higher level at 24 hours (Fig. 1D). This was accompanied by a concomitant enlargement of the $NADP^+$ pool (Fig. 1D). Similarly, when pancreatic cancer MIA PaCa-2 cells were cultured in suspension, as ROS levels rose and the NADPH/$NADP^+$ ratio declined, both NADPH and $NADP^+$ pools were enlarged (fig. S1, A to D).

To evaluate whether NADP(H) pool expansion is a general response of pancreatic cancer cells to redox stress, we treated PANC-1 cells cultured on adherent plates with hydrogen peroxide (H_2O_2). H_2O_2 augmented NADPH and $NADP^+$ pools while elevating ROS levels and lowering the NADPH/$NADP^+$ ratio (Fig. 1, E to H). Likewise, treatment of adherent PANC-1 cells with the thiol-oxidizing agent diamide, which elicited strong oxidative stress, enlarged NADPH and $NADP^+$ pools (fig. S1, E to H).

NADK1 is important for NADP(H) pool expansion

The expansion of NADPH and $NADP^+$ pools under various oxidative stress conditions prompted us to investigate both its causes and consequences. The most direct way to simultaneously increase NADPH and $NADP^+$ pools is through NADK, which catalyzes de novo $NADP^+$ biosynthesis from NAD^+ (*19*). We knocked down NADK1 and NADK2 individually in PANC-1 cells by means of small interfering RNA (siRNA). Knocking down NADK2 moderately reduced the basal levels of NADPH and $NADP^+$ in adherent cells (~10% reduction) but did not prevent their increase following matrix detachment (Fig. 1, I and J). By contrast, knocking down NADK1 not only reduced the basal levels of NADPH and $NADP^+$ but also prevented the increase in NADPH nearly completely and the increase in $NADP^+$ substantially in matrix-detached cells (Fig. 1, A and D). Similar effects of NADK1 knockdown were observed in MIA PaCa-2 cells (fig. S1, A and D). Moreover, knocking down NADK1 effectively blocked the increase in NADPH and $NADP^+$ levels in PANC-1 cells treated with H_2O_2 (Fig. 1, E and H) or diamide (fig. S1, E and H). In addition, we knocked out NADK1 in PANC-1 cells using CRISPR-mediated genome editing. Deletion of NADK1 with two independent single-guide RNAs (sgRNAs) decreased NADPH and $NADP^+$ levels and the NADPH/$NADP^+$ ratio in adherent cells and prevented their increase in suspension cells (fig. S1, I to K). Conversely, forced NADK1 expression increased NADPH and $NADP^+$ levels and the NADPH/$NADP^+$ ratio in detached PANC-1 cells (Fig. 1, K to M). Collectively, these results suggest that while both NADK1 and NADK2 contribute to the basal levels of $NADP^+$ and NADPH, NADK1 is primarily responsible for the increase in the overall NADP(H) pool under oxidative stress conditions.

To evaluate whether oxidative stress accentuates the metabolic flux to NAD^+ and $NADP^+$, we performed an isotope tracing experiment. In many tumor cell lines, NAD^+ is mainly generated by the salvage pathway using NAM as the substrate (Fig. 1N) (*39*). We cultured PANC-1 cells in medium supplemented with 2,6,7-$^{13}C_3$- (pyridyl-^{15}N)-NAM and measured M + 4 isotopomers of NAD^+ and $NADP^+$ by liquid chromatography–mass spectrometry (LC-MS) (Fig. 1N) (*35*, *39*). Following matrix detachment, the conversion of NAM to NAD^+ and $NADP^+$ was increased by ~30 to 40% in PANC-1 cells (Fig. 1O). Knocking down NADK1 not only reduced the basal flux from NAM to NAD^+ and $NADP^+$ in matrix-attached cells but also largely prevented its increase in matrix-detached cells (Fig. 1O). The specificity of this assay was shown by the observation that production of M + 4 isotopomers of NAD^+ and $NADP^+$ was strongly reduced by FK866, an inhibitor of the rate-limiting enzyme NAM phosphoribosyltransferase (NAMPT) (fig. S1L). These results indicate that in response to oxidative stress, pancreatic cancer cells enlarge the total NADP(H) pool by increasing the metabolic flux through NADK1.

When cultured in suspension, NADK1-knockdown and NADK1-knockout PANC-1 cells contained higher ROS levels and a lower NADPH/$NADP^+$ ratio (Fig. 1, B and C, and fig. S1, K and M) and displayed a reduction in cell viability (Fig. 1P and fig. S1N), compared to their corresponding control cells. Similarly, NADK1-knockdown MIA PaCa-2 cells showed aggravated redox stress and worsened viability when cultured in suspension (fig. S1, B, C, and O). In addition, knockdown of NADK1 rendered PANC-1 cells less able to withstand oxidative stress elicited by H_2O_2 (Fig. 1, F and G) or diamide (fig. S1, F and G) and more susceptible to their proapoptotic effect (Fig. 1Q and fig. S1P). Conversely, forced expression of NADK1 ameliorated oxidative stress and promoted the survival of PANC-1 cells cultured in suspension (Fig. 1, M, R, and S). Collectively, these results indicate that pancreatic cancer cells rely on an increase in NADK1-mediated de novo $NADP^+$ synthesis to withstand redox stress.

Expansion of NADP(H) pools upon redox stress conditions is dependent on G6PD

Despite the importance of an increased metabolic flux through NADK1 for redox balance, levels of NADK1 protein remained

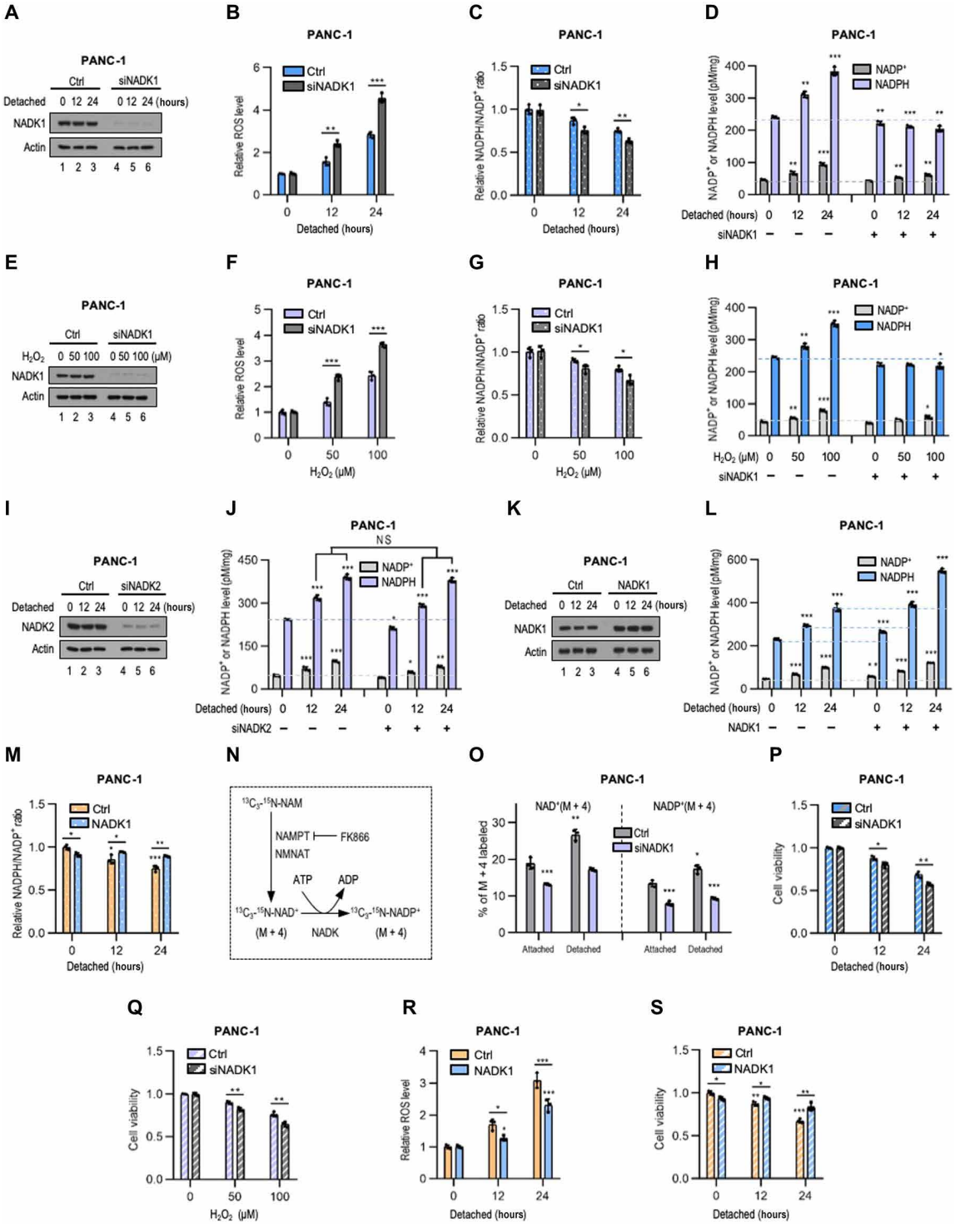

Fig. 1. Expansion of NADP$^+$ and NADPH pools following oxidative stress and its dependence on NADK1, but not NADK2. (**A** to **J**, **P**, and **Q**) PANC-1 cells treated with control, NADK1 (A to H, P, and Q), or NADK2 (I and J) siRNA were cultured under matrix-attached (0 hour) or matrix-detached conditions (A to D, I, J, and P) or treated with a different dose of H_2O_2 (E to H and Q). Cells were assayed for protein expression (A, E, and I), ROS content (B and F), the NADPH/NADP$^+$ ratio (C and G), NADP$^+$ and NADPH levels (normalized by total protein) (D, H, and J), and viability (P and Q). (**K** to **M**, **R**, and **S**) Control or NADK1-overexpressing PANC-1 cells were cultured under indicated conditions and assayed for protein expression (K), NADP$^+$ and NADPH levels (L), the NADPH/NADP$^+$ ratio (M), ROS content (R), and viability (S). (**N**) Schematic diagram of isotopic tracing for in vivo NADK function. NMNAT, NAM mononucleotide adenylyl transferase. (**O**) PANC-1 cells treated with control or NADK1 siRNA were cultured under matrix-attached (0 hours) or matrix-detached condition for 9 hours. Cells were incubated for another 3 hours with $^{13}C_3$-^{15}N-NAM and assayed for the M + 4 isotopomers of NAD$^+$ (left) and NADP$^+$ (right). Data are means ± SD ($n = 3$) and are representative of three independent experiments. *$P < 0.05$, **$P < 0.01$, and ***$P < 0.001$; NS, not significant; two-way analysis of variance (ANOVA) for (D), (H), (J), (L), and (O) and unpaired Student's t test for the rest.

unchanged under matrix detachment and other stress conditions (Fig. 1, A, E, and K, and fig. S1, A, E, and I). We recently observed that G6PD can directly bind to and stimulate the activity of NADK1 (*14*). Therefore, we examined whether G6PD is up-regulated under oxidative stress conditions and, if so, whether it effectuates the increased flux through NADK1. Upon matrix detachment, levels of G6PD markedly increased in PANC-1 cells (Fig. 2A), consistent with previous observations on other cell types (*7*, *14*). This increase was likely due to enhanced *G6PD* expression, as *G6PD* mRNA levels also rose (Fig. 2B). Similarly, levels of G6PD protein and mRNA increased in response to H_2O_2 or diamide treatment (fig. S2, A and B).

G6PD interacted with NADK1 in PANC-1 cells, as shown by a coimmunoprecipitation assay (fig. S2C), and this interaction was enhanced upon matrix detachment or H_2O_2 treatment (fig. S2, C and D). The observed G6PD-NADK1 interaction and its increase were abolished upon depletion of G6PD, underscoring the specificity of the assay (fig. S2, C and D). In G6PD-depleted cells, NADPH levels no longer increased and instead moderately declined, following matrix detachment (Fig. 2, A and C). $NADP^+$ levels were elevated in these cells but to an extent less than that in control cells (Fig. 2C). The reduction in NADPH and increase in $NADP^+$ levels were likely due to enhanced NADPH oxidation, as the total NADP(H) pool remained virtually unchanged (Fig. 2C). Compared to control cells, G6PD-depleted PANC-1 cells also displayed a further decline in the NADPH/$NADP^+$ ratio (by ~20 to 30%), a stronger increase in ROS content (by ~120%), and an additional reduction in viability (by ~30 to 35%) (Fig. 2, D to F). Using the isotope tracing assay, we observed that depletion of G6PD, while having a minimal effect on the basal NAD^+ and $NADP^+$ syntheses in matrix-attached cells, largely prevented their increase in matrix-detached cells (Fig. 2G).

To verify the role of G6PD, we used a recently developed, potent inhibitor of G6PD (G6PDi-1) (fig. S2E) (*40*). G6PDi-1 had a minimal effect on matrix-attached PANC-1 cells; however, it noticeably reduced $NADP^+$ and NADPH pools and the NADPH/$NADP^+$ ratio, elevated ROS levels, and worsened the viability of matrix-detached cells (fig. S2, F to I). Active G6PD dimer and tetramer, but not the inactive monomer, interact with and activate NADK1 (*14*). G6PDi-1 prevented the formation of active G6PD dimer/tetramer (fig. S2, J and K) and blocked the G6PD-NADK1 interaction (fig. S2L). Thus, G6PDi-1 likely exacerbates redox stress in part due to a reduction in NADK1 activity.

Conversely, forced G6PD expression noticeably increased the basal NADPH and $NADP^+$ levels in matrix-attached MIA PaCa-2 cells (by ~70 and 60%, respectively) and further elevated these metabolites in matrix-detached cells (Fig. 2, H and I). Forced G6PD expression also led to a higher NADPH/$NADP^+$ ratio, a lower ROS content, and better viability of matrix-detached cells (Fig. 2, J to L). These effects of G6PD were dependent on NADK1, as they were nearly completely abolished upon NADK1 knockdown (Fig. 2, M to O, and fig. S2, M and N).

To further investigate the importance of G6PD-mediated activation of NADK1, we used a G6PD mutant, $G6PD^{K171Q}$ (*21*), which loses the catalytic activity but retains the ability to bind to and activate NADK1 (fig. S2O) (*14*). In cells, $G6PD^{K171Q}$ is less able to enlarge the NADPH pool compared to wild-type G6PD and unable to increase the NADPH/$NADP^+$ ratio due to its inability to convert $NADP^+$ to NADPH (*14*). To compensate for this lower activity, we expressed $G6PD^{K171Q}$ at a higher level than G6PD in MIA PaCa-2 cells (Fig. 2P). When cultured on monolayers, $G6PD^{K171Q}$-expressing cells were able to maintain higher NADPH levels, akin to G6PD-expressing cells (Fig. 2Q), although they did not exhibit an elevated NADPH/$NADP^+$ ratio due to a simultaneous increase in $NADP^+$ (fig. S2P). Upon matrix detachment, $G6PD^{K171Q}$-expressing cells exhibited a higher NADPH/$NADP^+$ ratio, a lower ROS content, and better viability than control cells (Fig. 2, R to T). These effects of $G6PD^{K171Q}$ were comparable with those of G6PD. Thus, the robust antioxidant effect of G6PD overexpression is largely due to an increase in de novo $NADP^+$ production rather than the conversion of $NADP^+$ to NADPH. Collectively, these results suggest that under oxidative stress conditions, G6PD up-regulation activates NADK1 to bolster $NADP^+$ synthesis, promoting redox balance and cell viability.

Similar to NADK1, levels of NAMPT and NMNAT1 (NAM mononucleotide adenylyl transferase 1), two other essential upstream enzymes of $NADP^+$ de novo synthesis pathway, remained unchanged following matrix detachment (fig. S3, A to C). However, unlike NADK1, the activity of NAMPT and NMNAT1 was not altered when G6PD was knocked down (fig. S3, A to C). These results further support the notion that NADK1 is the focal point of regulation for de novo $NADP^+$ synthesis.

NADK1 is phosphorylated and activated by AKT and PKC (*35*, *36*). AKT signaling was attenuated in PANC-1 cells upon matrix detachment (fig. S3A), leading to a decrease in NADK1 phosphorylation (fig. S3D). By contrast, PKC signaling was activated following matrix detachment (fig. S3A), resulting in an increase in NADK1 phosphorylation (fig. S3E). Nevertheless, in cells devoid of G6PD, the net effect of AKT- and PKC-mediated phosphorylation, as well as other potential regulatory mechanisms, was a slight reduction in NADK1 enzyme activity (fig. S3, F to H). These results further indicate that G6PD up-regulation is primarily responsible for NADK1 activation under oxidative stress conditions.

Unique ability of G6PD in stimulating de novo $NADP^+$ synthesis

To evaluate a potential role for other NADPH-regenerating enzymes in stimulating NADK1 activity, we examined the expression of the second NADPH-producing enzyme in the oxidative PPP, 6-phosphogluconate dehydrogenase (6PGD), the tricarboxylic acid (TCA) cycle–associated malic enzymes (MEs) and isocitrate dehydrogenases (IDHs), and the one-carbon metabolic enzymes aldehyde dehydrogenase 1 family member L1 (ALDH1L1) and L2 (ALDH1L2). mRNA and protein levels of IDH1, ALDH1L2, and, to a less extent, IDH2 were increased in matrix-detached PANC-1 and MIA PaCa-2 cells, whereas levels of the other enzymes remained unchanged (fig. S4, A to D). Knockdown of IDH1 or ALDH1L2 in PANC-1 cells reduced the NADPH/$NADP^+$ ratio, elevated ROS content, and decreased cell viability, but these effects were not as strong as those elicited by knockdown of G6PD (fig. S4, E to H). Moreover, knockdown of IDH1 or ALDH1L2 did not impede the increase in the $NADP^+$ or NADPH pool in matrix-detached PANC-1 cells (fig. S4I). Forced expression of IDH1 or ALDH1L2, albeit elevating the NADPH/$NADP^+$ ratio as much as that of G6PD (fig. S4, J and K), failed to enlarge the $NADP^+$ or NADPH pool in matrix-attached PANC-1 cells (fig. S4L). Therefore, although some other NADPH-regenerating enzymes may also be important for maintaining the NADPH/$NADP^+$ ratio in unstressed cells, G6PD appears to be unique in its ability to stimulate de novo $NADP^+$ biosynthesis under oxidative stress conditions.

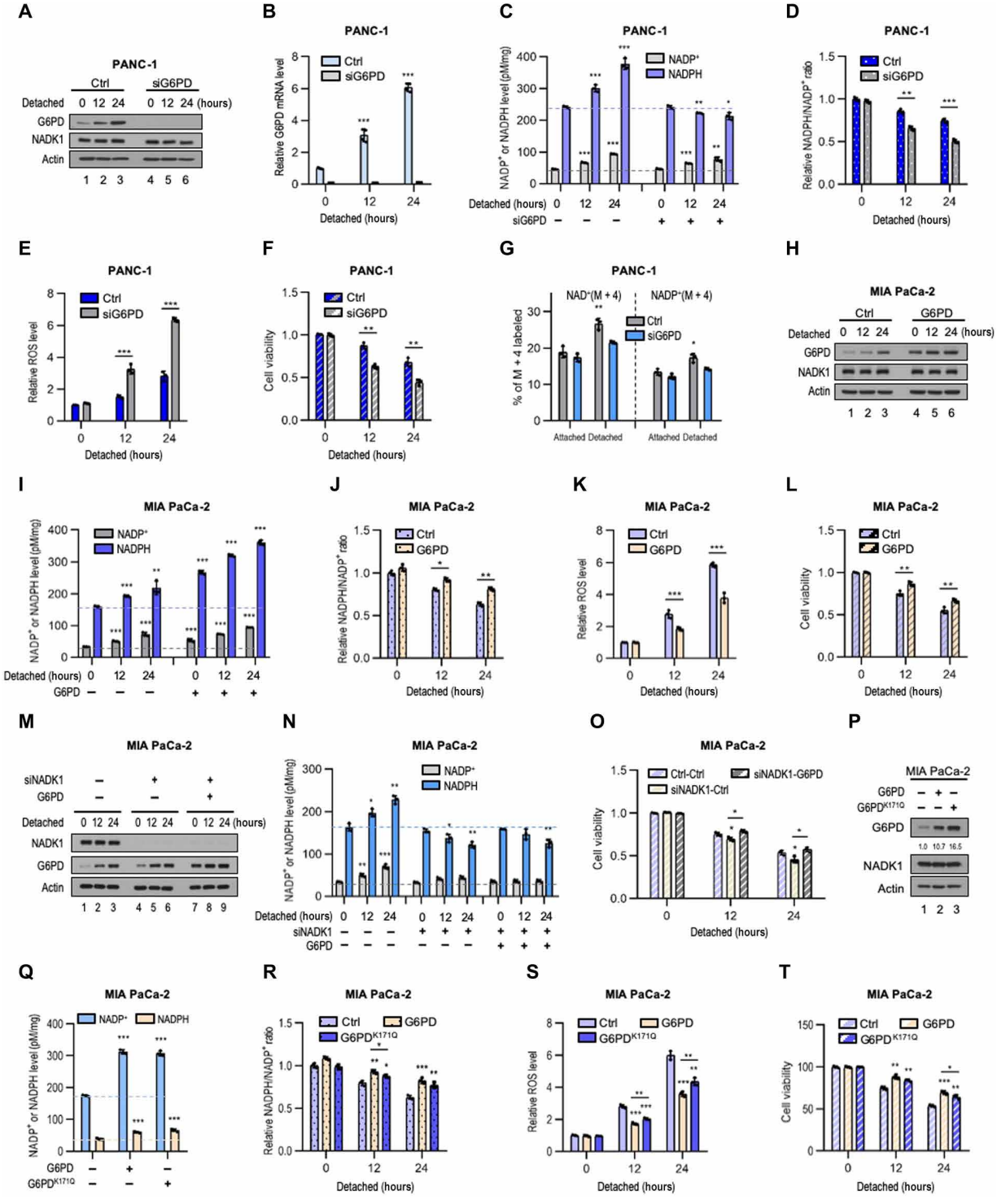

Fig. 2. G6PD is required for NADP(H) pool expansion under oxidative stress conditions. (**A** to **F**) PANC-1 cells treated with control or G6PD siRNA were cultured under indicated conditions and assayed for protein expression (A), G6PD mRNA levels (B), $NADP^+$ and NADPH pools (C), the NADPH/$NADP^+$ ratio (D), ROS content (E), and viability (F). (**G**) PANC-1 cells treated with control or G6PD siRNA were cultured under matrix-attached or matrix-detached condition for 9 hours. Cells were then incubated for another 3 hours with $^{13}C_3$-^{15}N-NAM and assayed for M + 4 isotopomers of NAD^+ and $NADP^+$. (**H** to **O**) Control and G6PD-overexpressing MIA PaCa-2 cells (H to L) or control and G6PD-overexpressing MIA PaCa-2 cells treated with control (–) or NADK1 (+) siRNA (M to O) were cultured under indicated conditions and assayed for protein expression (H and M), $NADP^+$ and NADPH levels (I and N), the NADPH/$NADP^+$ ratio (J), ROS content (K), and viability (L and O). (**P** to **T**) MIA PaCa-2 cells harboring G6PD, $G6PD^{K171Q}$, and control expression vectors were assayed for protein expression (P) and $NADP^+$ and NADPH levels (Q). Cells were also cultured under matrix-detached conditions for the indicated times and assayed for the NADPH/$NADP^+$ ratio (R), ROS content (S), and viability (T). Data are means ± SD [$n = 4$ for (B) and 3 for the rest] and are representative of three independent experiments. *$P < 0.05$, **$P < 0.01$, and ***$P < 0.001$; two-way ANOVA for (C), (G), (I), and (N) and unpaired Student's t test for the rest.

Role of endogenous G6PD in redox homeostasis

We recently showed that forced G6PD expression augments antioxidant defense capacity and nucleotide precursor availability, leading to oncogenic transformation of immortalized mouse and human cells (*14*). To investigate the role of endogenous G6PD, we performed LC–high-resolution MS (LC-HRMS)–based metabolomics on control and G6PD-knockdown PANC-1 cells that were cultured under matrix-attached and matrix-detached conditions (Fig. 3A). Following matrix detachment, control PANC-1 cells exhibited a noticeable increase in levels of NADPH and PPP intermediates (Fig. 3, B and C), consistent with the up-regulation of G6PD in these cells (Figs. 2A and 3A). These cells showed a reduction in the ratio of reduced glutathione (GSH) versus oxidized glutathione (GSSG) (Fig. 3D), and they contained less nucleoside triphosphates and diphosphates (Fig. 3C) and more nucleoside monophosphates (Fig. 3C), suggesting that these cells were experiencing both oxidative and energetic stresses. Control PANC-1 cells also consumed glucose and secreted lactate at a higher rate upon matrix detachment (Fig. 3, E and F), presumably due to impaired mitochondria respiration. In addition, they used more glutamine (Fig. 3G), consistent with previous observation that cancer cells may rely on glutamine to maintain redox balance during anchorage-independent growth (*15*).

Matrix-attached G6PD-knockdown cells showed a strong reduction in the G6PD product 6-phosphogluconic acid compared to control cells, as expected (Fig. 3C). Nevertheless, these cells displayed minimal or no changes in the GSH/GSSG ratio (Fig. 3D), levels of most metabolites including ribose 5-phosphate (Fig. 3C), glucose and glutamine consumption (Fig. 3, E and G), lactate excretion (Fig. 3F), or oxygen uptake (Fig. 3, H and I). Thus, in cells encountering minimal redox stress, the metabolic function of endogenous G6PD may be limited.

However, upon matrix detachment, energetic and oxidative stresses were aggravated in G6PD-knockdown cells compared to control cells, with a larger decline in the GSH/GSSG ratio and levels of nucleoside triphosphates and diphosphates (Fig. 3, C and D). Detached G6PD-knockdown cells also consumed more glucose but not glutamine (Fig. 3, E and G), excreted a higher amount of lactate (Fig. 3F), used less oxygen (Fig. 3, H and I), and directed fewer glucose molecules to the TCA cycle (Fig. 3J). Nevertheless, G6PD-knockdown and control cells synthesized DNA synthesis at a comparable rate (Fig. 3K). These results suggest that the main role of endogenous G6PD is to maintain redox balance.

Consistent with this notion, when grew in suspension and supplemented with the antioxidant *N*-acetyl cysteine (NAC), G6PD-knockdown PANC-1 cells showed similar NADPH/$NADP^+$ ratio, ROS content, and viability to control cells (fig. S5, A to D). Supplementation with NAC also restored redox balance and cell viability in matrix-detached PANC-1 cells treated with G6PDi-1 (fig. S5, E to H). Moreover, while G6PD overexpression afforded MIA PaCa-2 cells a strong antioxidant capacity and higher viability under matrix-detached conditions, these advantages were largely abolished by H_2O_2 treatment (fig. S5, I to L). Therefore, endogenous G6PD is critical for mitigating oxidative stress.

G6PD is activated by TAp73 under oxidative stress conditions

The data presented above show that G6PD is up-regulated in response to oxidative stress, leading to an increase in NADK1-mediated de novo $NADP^+$ biosynthesis. Next, we investigated the mechanism by which G6PD expression is activated by oxidative stress. We previously observed that TAp73 maintains G6PD expression in unstressed cells (*41*, *42*). However, the role of TAp73 in redox homeostasis is unknown. Notably, in matrix-detached PANC-1 cells, levels of TAp73 protein were augmented in parallel with those of G6PD protein (Fig. 4, A and B). Silencing TAp73 by siRNA not only reduced the basal levels of G6PD mRNA and protein in matrix-attached PANC-1 cells but also largely prevented their up-regulation following matrix detachment (Fig. 4, A and B). Under matrix detachment conditions, silencing TAp73 also abrogated the increase in de novo $NADP^+$ synthesis (Fig. 4C) and $NADP^+$ and NADPH pools (Fig. 4D), further reduced the NADPH/$NADP^+$ ratio (Fig. 4E) and elevated ROS levels (Fig. 4F), and worsened viability (Fig. 4G). Notably, these detrimental consequences of TAp73 silencing were largely rescued by G6PD overexpression (fig. S6, A to D).

Conversely, forced TAp73 expression substantially increased the basal G6PD levels in matrix-attached PANC-1 cells and further elevated them in matrix-detached cells (Fig. 4H). It also enlarged NADPH and $NADP^+$ pools, increased the NADPH/$NADP^+$ ratio, reduced ROS content in both matrix-attached and especially in matrix-detached cells (Fig. 4, I to K), and enhanced cell viability (Fig. 4L).

To confirm the generality of this effect of TAp73, we used several other human cancer cell lines, including colon cancer HCT116 cells, liver cancer HepG2 cells, and prostate cancer PC-3 cells. In each of these cell types, TAp73 protein levels rose following matrix detachment, correlating with an increase in G6PD protein levels (fig. S6, E to G). In addition, knocking down TAp73 noticeably reduced G6PD levels under matrix-attached and matrix-detached conditions (fig. S6, E to G). Moreover, TAp73 and G6PD levels increased in primary human mammary epithelial cells (HMECs) upon detachment (fig. S6H). Knocking down TAp73 largely prevented the increase in G6PD protein and mRNA levels in HMECs (fig. S6, H and I). This was accompanied by a higher redox stress and lower cell viability (fig. S6, J and K). Conversely, overexpressing TAp73 in HMECs augmented G6PD expression, reduced ROS content, and improved cell viability (fig. S6, L to N). Together, these results indicate that TAp73 activates G6PD expression in both normal and malignant cells following matrix detachment.

Moreover, treatment with H_2O_2 resulted in a correlative increase in TAp73 and G6PD in adherent U2OS, PANC-1, HCT116, HepG2, and PC-3 cells (Fig. 4M and fig. S6, O to R). In each of these cell lines, knocking down TAp73 effectively abrogated H_2O_2-induced G6PD expression. Knocking down TAp73 also reduced NADPH/$NADP^+$ ratio and exacerbated oxidative stress in H_2O_2-treated U2OS cells (Fig. 4, N and O). Similarly, treatment with diamide concurrently activated TAp73 and G6PD in U2OS cells (Fig. 4P) and HCT116 cells (fig. S6S), whereas knocking down TAp73 blocked G6PD up-regulation and aggravated redox stress in these cells (Fig. 4, P and Q, and fig. S6, S and T). Together, these results indicate that TAp73 activates G6PD expression in a wide range of cell types in response to various oxidative stress conditions.

NRF2 is an upstream regulator of TAp73

Next, we sought to determine the upstream regulators of TAp73. NRF2, a redox-responsive transcription factor, activates the expression of a wide range of antioxidant and detoxification genes, including *G6PD* (*31*, *32*). However, it is unclear whether NRF2 directly regulates *G6PD*. Given that TAp73 is probably a proximal transcription

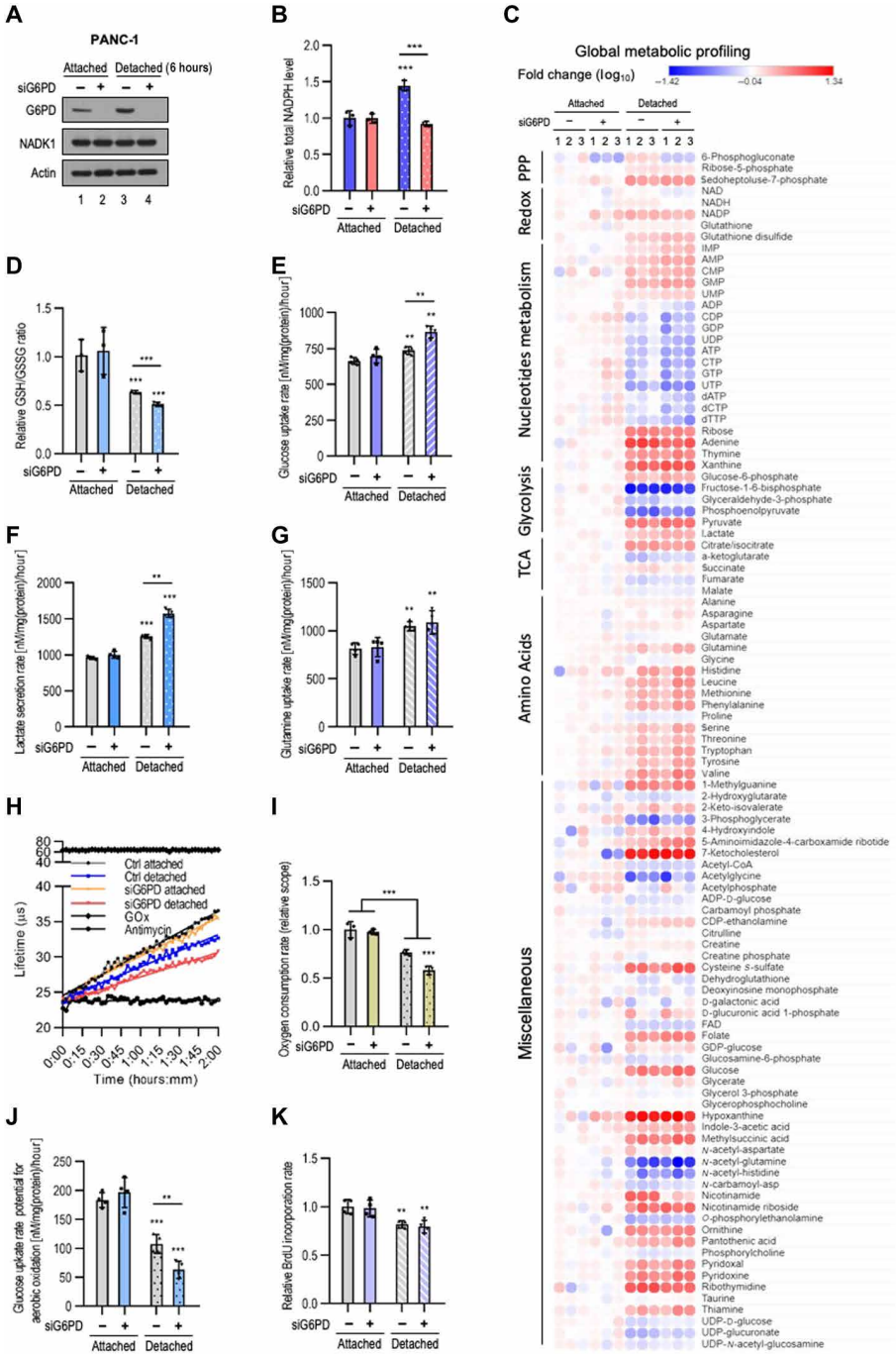

Fig. 3. Endogenous G6PD is essential for maintaining redox homeostasis. (**A** to **D**) PANC-1 cells treated with control (–) or G6PD (+) siRNA were cultured under matrix-attached or matrix-detached condition for 6 hours. Cells were assayed for protein expression (A), NADPH levels (B), and global metabolomics (C). Relative GSH/GSSG ratio (D) was replotted from (C) of the same conditions. The levels of metabolites were normalized by the total amount of protein in each sample. IMP, inosine 5′-monophosphate; AMP, adenosine 5′-monophosphate; CMP, cytidine 5′-monophosphate; GMP, guanosine 5′-monophosphate; UMP, uridine 5′-monophosphate; ADP, adenosine 5′-diphosphate; CDP, cytidine 5′-diphosphate; GDP, guanosine diphosphate; UDP, uridine 5′-diphosphate; CTP, cytidine 5′-triphosphate; GTP, guanosine 5′-triphosphate; UTP, uridine 5′-triphosphate; dATP, 2′-deoxyadenosine 5′-triphosphate; dCTP, 2′-deoxycytidine 5′-triphosphate; dTTP, 3′-deoxythymidine 5′-triphosphate; CoA, coenzyme A; FAD, flavin adenine dinucleotide. (**E** to **K**) PANC-1 cells treated with control (–) or G6PD (+) siRNA were cultured under matrix-attached or matrix-detached condition for 6 hours. Cells were assayed for glucose (E) and glutamine (G) uptake, lactate secretion (F), oxygen consumption (H and I), and DNA synthesis by 5-bromo-2′-deoxyuridine (BrdU) incorporation (K). The glucose or glutamine uptake rate and lactate secretion rate were normalized by the total amount of protein in each sample. BrdU incorporation rate was normalized by the cell number of each sample. Oxygen consumption rate in (I) was determined by the relative scope of lifetime (in microseconds) in (H) of phosphorescent oxygen probe. Glucose uptake rate potential for aerobic oxidation (J) was calculated from the glucose uptake rate (E) and lactate secretion rate (F) of each sample. Data are means ± SD of representative result [$n = 3$ for (B) to (D) and (I) and 4 for the rest] and are representative of two (C and D) or three (the rest) independent experiments. $^{**}P < 0.01$ and $^{***}P < 0.001$; two-way ANOVA for (I) and unpaired Student's t test for the rest.

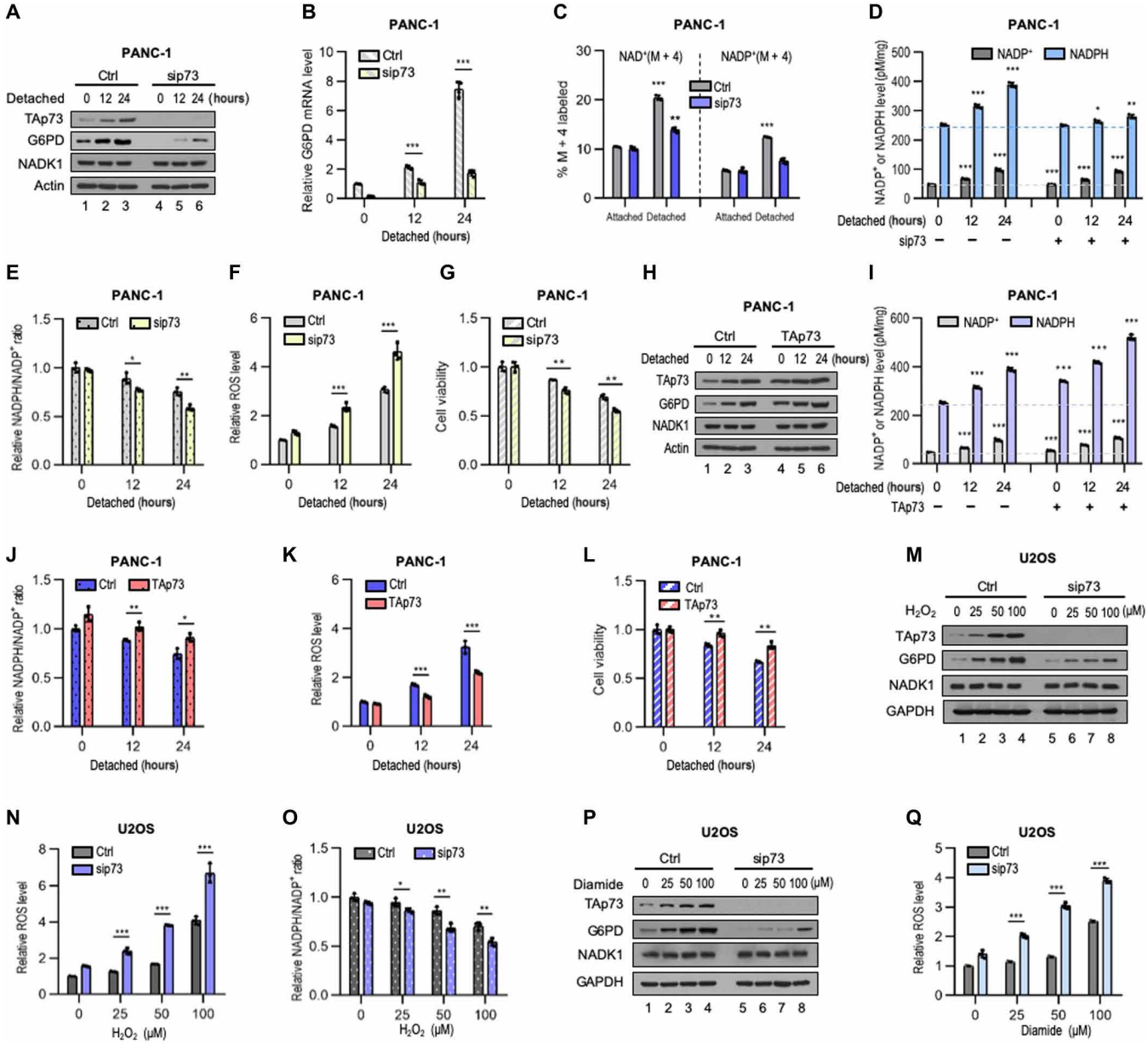

Fig. 4. TAp73 is a redox-responsive and proximal transcriptional factor of G6PD. (**A** to **L**) PANC-1 cells treated with control or p73 siRNA (A to G) or harboring control or TAp73 expression vector (H to L) were cultured under matrix-attached or matrix-detached conditions for the indicated durations or 12 hours. Cells were assayed for protein expression (A and H), G6PD mRNA levels (B), $NADP^+$ and NADPH levels (D and I), the NADPH/$NADP^+$ ratio (E and J), ROS content (F and K), and viability (G and L). For (C), cells were additionally cultured for 2 hours in the presence of $^{13}C_3$-^{15}N-NAM and assayed for M + 4 isotopomers of NAD^+ and $NADP^+$ by LC-MS. (**M** to **Q**) Protein expression (M and P), ROS content (N and Q), and the NADPH/$NADP^+$ ratio (O) in control and p73-knockdown U2OS cells treated with different doses of H_2O_2 (M to O) or diamide (P and Q) for 48 hours. Data are means ± SD [$n = 4$ for (B) and 3 for the rest] and are representative of three independent experiments. *$P < 0.05$, **$P < 0.01$, and ***$P < 0.001$; two-way ANOVA for (C), (D), and (I) and unpaired Student's t test for the rest.

factor for G6PD, we investigated the possibility that NRF2 may be an activator of TAp73. When PANC-1 cells were detached from monolayers, NRF2 was increased in a time-dependent manner, in parallel with TAp73 and G6PD (Fig. 5A). Knocking down NRF2 by siRNA attenuated the increase in TAp73 and G6PD (Fig. 5A). This, in turn, reduced de novo $NADP^+$ synthesis, NADP(H) pool size, the NADPH/$NADP^+$ ratio, and cell viability while elevating ROS content (Fig. 5, B to F). Similarly, knocking down NRF2 lessened the upregulation of TAp73 and G6PD in H_2O_2-treated U2OS cells (Fig. 5G).

Upon TAp73 knockdown, NRF2 levels were elevated in PANC-1, HCT116, HepG2, and PC-3 cells as well as HMECs even when these cells were cultured in monolayers in the absence of exogenous oxidants (fig. S6, E to H and O to S), probably due to a higher ROS content in the absence of TAp73. Following matrix detachment or H_2O_2/diamide treatment, NRF2 expression was increased more strongly in TAp73-knockdown cells than in control cells (fig. S6, E to H and O to S). Despite the higher levels of NRF2, G6PD levels remained low in TAp73-knockdown cells (fig. S6, E to H and O to S).

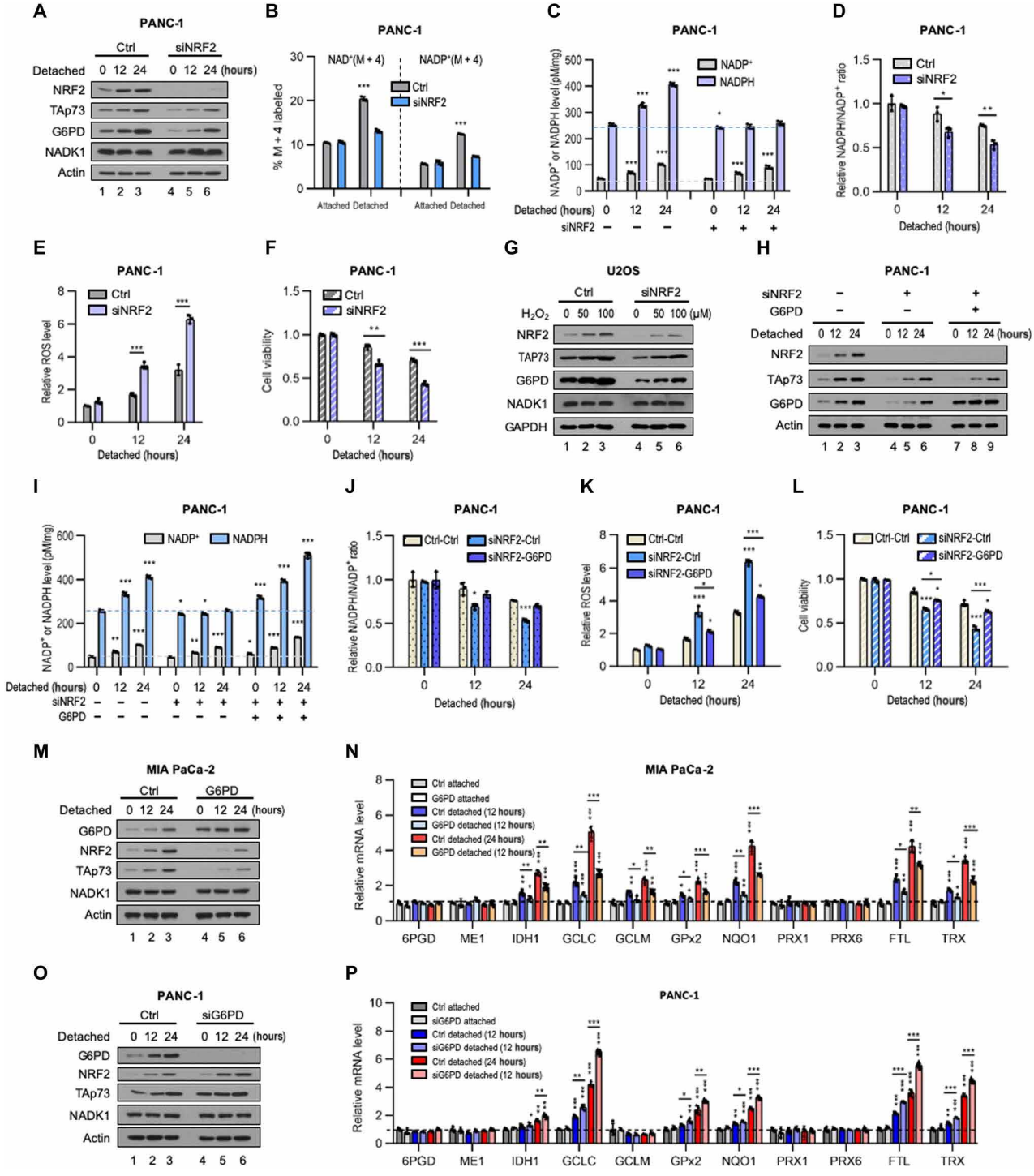

Fig. 5. The TAp73-G6PD axis is a major downstream effector of NRF2. (**A** to **G**) PANC-1 (A to F) or U2OS (G) cells treated with control or NRF2 siRNA were cultured under matrix-attached or matrix-detached conditions as indicated or for 12 hours (A to F) or exposed to different doses of H_2O_2 for 48 hours (G). Cells were assayed for protein expression (A and G), isotopic incorporation (B), $NADP^+$ and NADPH levels (C), the NADPH/$NADP^+$ ratio (D), ROS content (E), and viability (F). The isotopic tracing experiment in (B) was done together with that in Fig. 4C. (**H** to **L**) PANC-1 cells harboring control or G6PD expression vectors were treated with control or NRF2 siRNA and cultured under indicated conditions. Cells were assayed for protein expression (H), $NADP^+$ and NADPH levels (I), the NADPH/$NADP^+$ ratio (J), ROS content (K), and viability (L). (**M** to **P**) Protein expression (M and O) and mRNA levels of NRF2 target genes involved in antioxidant defense (N and P) in MIA PaCa-2 cells harboring control or G6PD expression vectors (M and N) or PANC-1 cells treated with control or G6PD siRNA (O and P) that were cultured under indicated conditions. Data are means ± SD [$n = 4$ for (N) and (P) and 3 for the rest] and are representative of three independent experiments. *$P < 0.05$, **$P < 0.01$, and ***$P < 0.001$; two-way ANOVA for (B), (C), and (I) and unpaired Student's t test for the rest. GCLC, glutamate-cysteine ligase catalytic subunit; GCLM, glutamate-cysteine ligase modifier subunit; GPx2, glutathione peroxidase 2; NQO1, NAD(P)H quinone dehydrogenase 1; PRX1, Peroxiredoxin 1; FTL, ferritin light chain; TRX, thioredoxin.

Collectively, these results indicate that TAp73 mediates the stimulatory effect of NRF2 on G6PD.

To evaluate the role of the TAp73-G6PD axis in NRF2-directed antioxidant response, we overexpressed G6PD in PANC-1 cells to levels comparable to those under redox stress conditions (Fig. 5H). In these G6PD-overexpressing PANC-1 cells where NADP and NADPH pools were noticeably enlarged (Fig. 5I), the effect of NRF2 knockdown on the NADPH/$NADP^+$ ratio, ROS content, and cell viability was much attenuated compared to that in control cells (Fig. 5, J to L). Moreover, in G6PD-overexpressing MIA PaCa-2 cells, levels of NRF2 and many of its target genes were noticeably reduced under both matrix-attached and matrix-detached conditions (Fig. 5, M and N). Still, these cells exhibited an augmented ability to withstand oxidative stress (Fig. 2, H to L). Conversely, in G6PD-knockdown PANC-1 cells, expression of NRF2 and its target genes was increased (Fig. 5, O and P). However, these cells exhibited higher redox stress and lower cell survival when detached from monolayers (Fig. 2, A to F). Collectively, these results indicate that the TAp73-G6PD axis is a major effector for NRF2-mediated antioxidant response.

NRF2 stabilizes the TAp73 protein

Although NRF2 knockdown reduced TAp73 protein levels in PANC-1 and U2OS cells (Fig. 5, A and G), it did not decrease, and instead moderately increased, TAp73 mRNA levels (Fig. 6, A and B). Thus, NRF2 may regulate TAp73 through a posttranscriptional mechanism. Consistent with this notion, a cycloheximide (CHX) chase experiment showed that NRF2 knockdown accelerated the degradation of endogenous TAp73 protein (Fig. 6, C and D), as well as exogenous TAp73 that was expressed from a heterologous promoter (Fig. 6, E and F). This effect of NRF2 knockdown was largely prevented by the proteasome inhibitor *N*-carbobenzyloxy-L-leucyl-L-leucyl-L-leucinal (MG132) (Fig. 6, G and H). Moreover, knocking down NRF2 increased TAp73 ubiquitination (Fig. 6I). Conversely, forced NRF2 expression increased steady-state levels of TAp73 and prolonged its half-life (Fig. 6, J and K). In contrast, forced expression of NRF1, another member of the NRF family (*43*), did not affect levels or stability of TAp73 and G6PD (Fig. 6, L and M). Therefore, NRF2 stabilizes TAp73 by preventing its proteasomal degradation.

NRF2 inhibits the expression of PIRH2

The activity of TAp73 is modulated by a number of proteins, including PML, p300, c-Abl, c-Jun, SUMO-1, and NEDL2 (*44*). Nevertheless, knockdown of NRF2 did not alter the expression or activation of these proteins in PANC-1 or U2OS cells (Fig. 7A). Several ubiquitin E3 ligases—including itchy E3 ubiquitin protein ligase (Itch), tripartite motif containing 33 (TRIM33), mouse double minute 2 (MDM2), and PIRH2—were previously implicated in TAp73 degradation (*45*–*47*). Knocking down NRF2 increased protein and mRNA levels of endogenous PIRH2, but not the other E3 ligases, in PANC-1 and U2OS cells (Fig. 7, B to D). Conversely, forced NRF2 expression decreased levels of endogenous PIRH2 (Fig. 7, E to H) but not exogenous Flag-PIRH2 that was expressed from a heterologous promoter (Fig. 7I). These results indicate that NRF2 inhibits the expression of the *PIRH2* gene.

Overexpressing PIRH2 decreased TAp73 levels in PANC-1 and U2OS cells. This effect was observed in both control cells and NRF2-overexpressing cells where TAp73 was stabilized (Fig. 7, E and F). Conversely, depleting PIRH2 increased TAp73 levels in both control cells and NRF2-knockdown cells where TAp73 was destabilized (Fig. 7, E and F) and reduced TAp73 ubiquitination (Fig. 6I). PIRH2 interacted with TAp73, as shown by a coimmunoprecipitation assay (Fig. 7J). The PIRH2-TAp73 interaction declined upon forced NRF2 expression (Fig. 7J). Knocking down PIRH2 also increased de novo $NADP^+$ synthesis, the total NADP(H) pool, and the NADPH/$NADP^+$ ratio and reduced ROS levels (Fig. 7, K to O) while promoting cell survival under matrix-detached conditions (Fig. 7P). These results confirm that PIRH2 binds to and promotes the degradation of TAp73, reducing cellular capability to maintain redox balance.

Inspection of the human *PIRH2* gene sequence revealed that at least three putative NRF2-binding motifs, also known as antioxidant response elements (AREs), are present near the transcription start site (Fig. 7, Q and R). A chromatin immunoprecipitation (ChIP) assay suggested that NRF2 might bind to the genomic region encompassing one of these sites (ARE3) (Fig. 7S). In a reporter gene assay, NRF2 inhibited the expression of the luciferase gene driven by a genomic fragment that contained all three wild-type AREs but not a fragment in which ARE3 was mutated (Fig. 7T). Collectively, these results indicate that NRF2 suppresses *PIRH2* expression, thereby stabilizing TAp73.

E2F1 activates *TAp73* expression in response to oxidative stress

In matrix-detached PANC-1 and U2OS cells where TAp73 protein was stabilized, *TAp73* mRNA was also induced (Fig. 6, A and B). Knocking down NRF2 increased, rather than decreased, *TAp73* transcript (Fig. 6, A and B). Thus, an NRF2-independent mechanism may regulate *TAp73* expression under redox stress conditions. A previous study showed that upon DNA damage, the checkpoint kinases CHK1 and CHK2 stabilize the transcription factor E2F1, which then directs the expression of *p73*, including the TA isoform (*48*). However, it is unknown whether E2F1 regulates TAp73 in response to oxidative stress. Notably, levels of E2F1 were increased along with those of TAp73, NRF2, and G6PD in PANC-1 cells following matrix detachment (Fig. 8A) or treatment with H_2O_2 or diamide (fig. S7, A and B). The activation of E2F1 was likely due to oxidative stress–induced DNA damage in these cells, as shown by phosphorylation of γ-H2AX (S139) and activation of CHK1 (Fig. 8A and fig. S7, A and B).

Knocking down E2F1 reduced TAp73 mRNA and protein levels in adherent cells and abrogated their increase upon cell detachment (Fig. 8, A and B). This was accompanied by a strong decline in both basal and detachment-induced G6PD protein and mRNA levels (Fig. 8, A and B). The decrease in TAp73 and G6PD upon E2F1 knockdown occurred despite a modest increase in NRF2 (Fig. 8A), again indicating that the effect of E2F1 on TAp73 is independent of NRF2. Together, these results show that E2F1 activates *TAp73* expression in cells experiencing oxidative stress.

In contrast to control cells, E2F1-knockdown cells were unable to accentuate de novo $NADP^+$ synthesis and expand $NADP^+$ and NADPH pools following matrix detachment (Fig. 8, C and D). They also displayed a reduced NADPH/$NADP^+$ ratio (Fig. 8E), an increased ROS content (Fig. 8F), and worsened viability (Fig. 8G). PANC-1 cells devoid of both NRF2 and E2F1 contained very low basal levels of TAp73 and G6PD proteins and were unable to up-regulate them following matrix detachment (Fig. 8H). Thus, E2F1-mediated increase in *TAp73* mRNA, similar to NRF2-mediated stabilization of TAp73 protein, contributes to NADP(H) pool expansion and antioxidant defense.

Collectively, these results reveal a cellular redox regulatory network that culminates in G6PD-mediated increase in de novo $NADP^+$

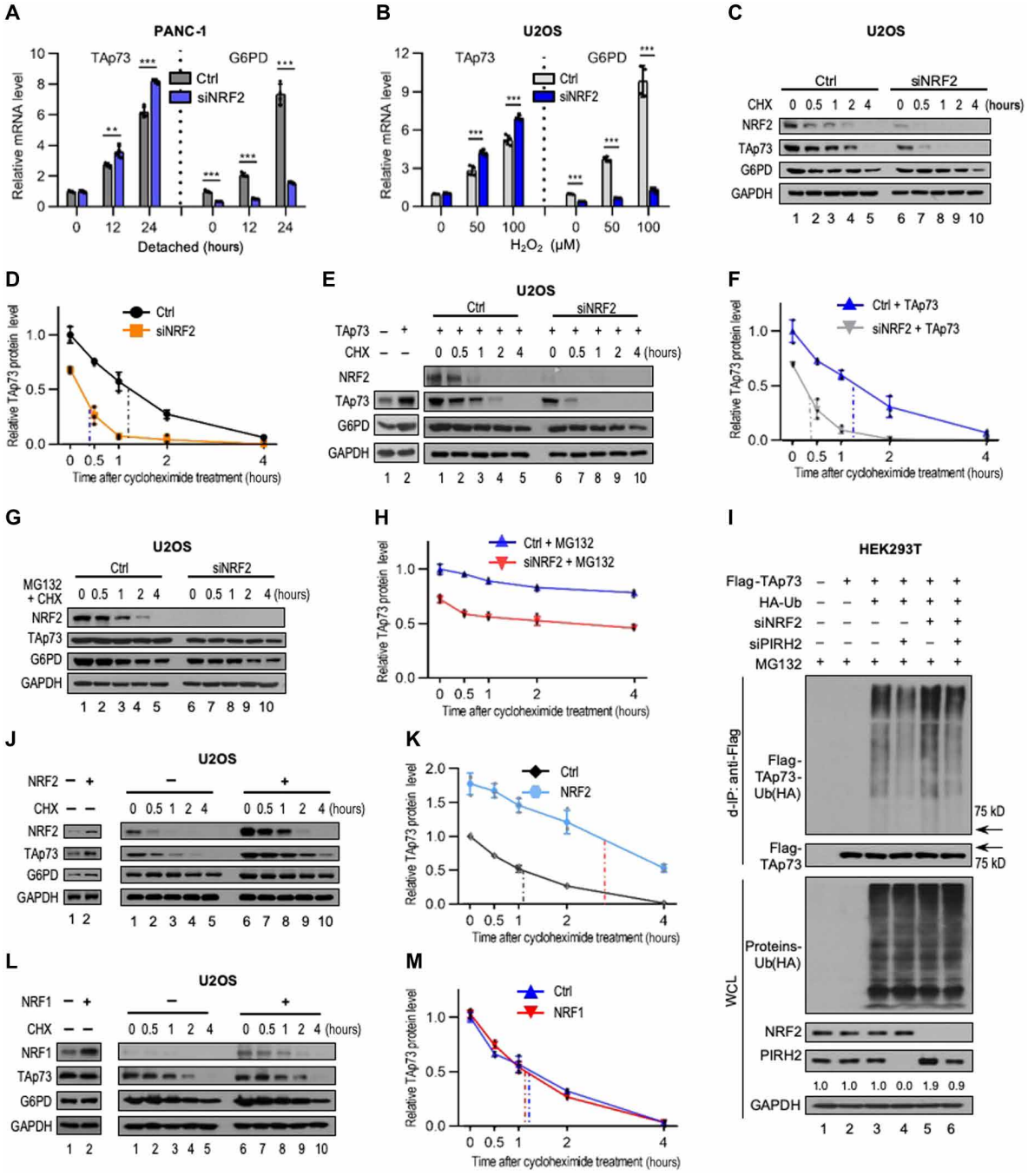

Fig. 6. NRF2 regulates the stability of the TAp73 protein. (**A** and **B**) TAp73 and G6PD mRNA levels in control and NRF2-knockdown PANC-1 (A) and U2OS (B) cells cultured under matrix-detached conditions for the indicated durations or treated with the indicated doses of H_2O_2. (**C** to **H**) U2OS cells (C, D, G, and H) or TAp73-overexpressing U2OS cells (E and F) were treated with control or NRF2 siRNA (C to H) in the presence of CHX alone (C to F) or CHX plus MG132 (G and H) as indicated. Shown are representative immunoblots (C, E, and G) and quantification of relative TAp73/glyceraldehyde-3-phosphate dehydrogenase (GAPDH) ratio in each sample, with the half-life of TAp73 indicated by dashed vertical lines (D, F, and H). (**I**) Human embryonic kidney (HEK) 293T cells were transfected with control siRNA, NRF2, or PIRH2 siRNA, along with hemagglutinin-ubiquitin (HA-Ub) and/or Flag-TAp73 expression vectors as indicated. Cells were treated with MG132 for 24 hours. After denaturing immunoprecipitation (d-IP) with the anti-Flag antibody, immunoprecipitates and whole-cell lysates were analyzed by Western blot. (**J** to **M**) Control, NRF2-overexpressing (J and K), and NRF1-overexpressing (L and M) U2OS cells were treated with CHX for the indicated times and assayed for protein expression (J and L) with quantification of relative TAp73/G6PD ratios shown in (K) and (M). Data are means ± SD [$n = 4$ for (A) and (B) and 3 for the rest] and are representative of three independent experiments. $^{**}P < 0.01$ and $^{***}P < 0.001$; unpaired Student's t test.

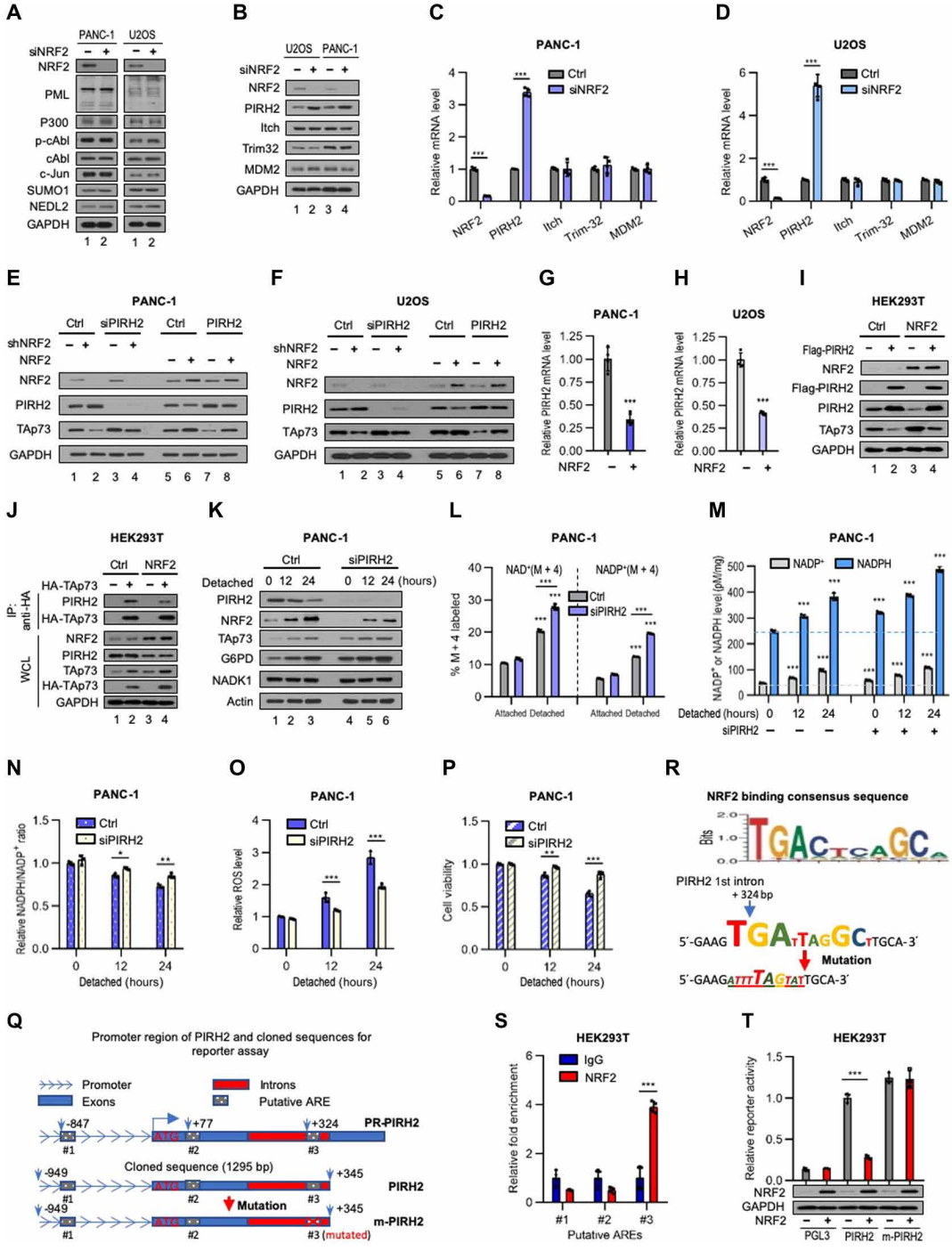

Fig. 7. NRF2 suppresses the expression of the *PIRH2* gene. (**A** to **D**) Protein (A and B) and mRNA (C and D) levels of TAp73 regulators in control and NRF2-knockdown PANC-1 or U2OS cells. (**E** to **H**) PIRH2 and TAp73 protein levels (E and F) and PIRH2 mRNA levels (G and H) in PANC-1 (E and G) and U2OS (F and H) cells with PIRH2 or NRF2 knockdown (by siRNA or shRNA) (E and F) or overexpression (E to H). (**I**) Flag-PIRH2 was transfected into control or NRF2-overexpressing HEK293T cells. Cells were assayed for protein expression. (**J**) HA-TAp73 was expressed in control or NRF2-overexpressing HEK293T cells. Interaction between HA-TAp73 and endogenous PIRH2 was detected by coimmunoprecipitation with anti-HA antibody. WCL, whole cell lysates. (**K** to **P**) Control and PIRH2-knockdown PANC-1 cells were cultured under matrix-detached conditions for the indicated times (K and M to P) or for 12 hours (L). Cells were assayed for protein expression (K), isotopic incorporation (L), $NADP^+$ and NADPH levels (M), the NADPH/$NADP^+$ ratio (N), ROS content (O), and viability (P). The isotopic tracing experiment in (L) was done together with that in Fig. 4C. (**Q**) Schematic diagram of the promoter region of PIRH2 (PR-PIRH2) as well as wild-type (PIRH2) and mutated (m-PIRH2) PIRH2 promoter sequences that were cloned into pGL3 vector. (**R**) NRF2-binding consensus sequence, sequence of putative ARE3, and its corresponding mutation. (**S**) ChIP assay of NRF2 binding to putative AREs in HEK293T cells. The enrichment fold was normalized with the corresponding immunoglobulin G (IgG) controls. (**T**) NRF2-mediated suppression of luciferase reporter gene driven by PIRH2 but not m-PIRH2 in HEK293T cells. Data are means ± SD [$n = 4$ for (C), (D), (G), and (H) and 3 for the rest] and are representative of two (R) and three (the rest) independent experiments. $^*P < 0.05$, $^{**}P < 0.01$, and $^{***}P < 0.001$; two-way ANOVA for (L) and (M) and unpaired Student's *t* test for the rest.

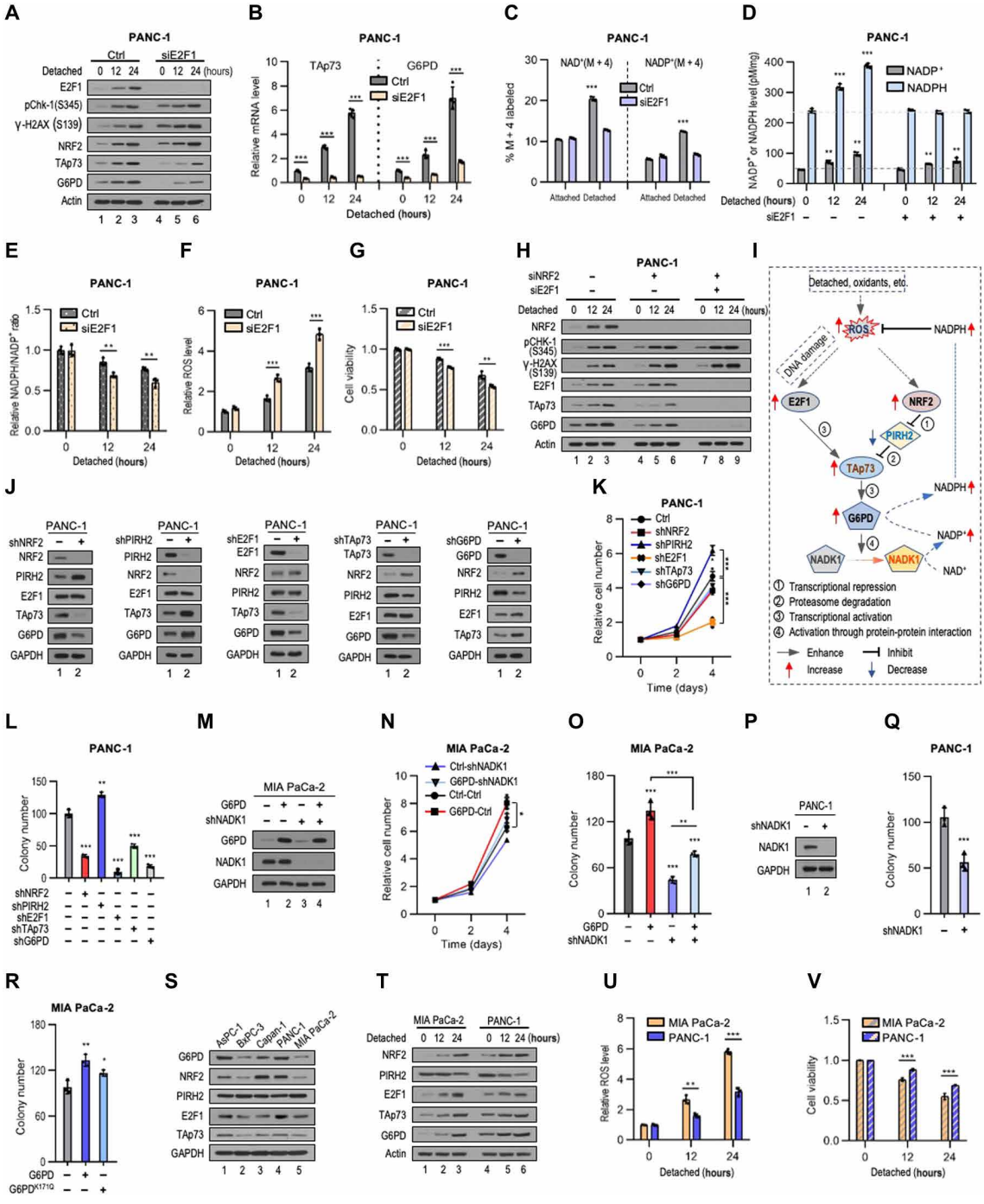

Fig. 8. Redox stress stimulates *TAp73* expression via the CHK1-E2F1 pathway, and both CHK1-E2F1 and NRF2-PIRH2 pathways regulate TAp73 and G6PD to promote anchorage-independent growth. (**A** to **H**) PANC-1 cells treated with control, E2F1, and/or NRF2 siRNAs were cultured under indicated conditions. Cells were assayed for protein expression (A and H), mRNA levels (B), isotope incorporation (C), $NADP^+$ and NADPH levels (D), the NADPH/$NADP^+$ ratio (E), ROS content (F), and viability (G). The isotopic tracing experiments in (C) were done together with that in Fig. 4C. (**I**) Schematic diagram shows signaling network that regulates G6PD for redox homeostasis. (**J** to **L**) PANC-1 cells with knockdown of the individual gene were assayed for protein expression (J), adherent growth (K), and soft-agar colony formation (L) (related to fig. S7C). (**M** to **O**) Control and G6PD-overexpressing MIA PaCa-2 cells with or without NADK1 knockdown were assayed for protein expression (M), adherent growth (N), and soft-agar colony formation (O) (related to fig. S7G). (**P** and **Q**) PANC-1 cells with or without NADK1 knockdown were assayed for protein expression (P) and soft-agar colony formation (Q) (related to fig. S7M). (**R**) Soft-agar colony formation by control, G6PD-overexpressing, and $G6PD^{K171Q}$-overexpressing MIA PaCa-2 cells. Protein expression is shown in Fig. 2P. (**S**) Levels of G6PD and its regulators in a panel of pancreatic cancer cells. (**T** to **V**) MIA PaCa-2 and PANC-1 cells were cultured under matrix-detached conditions for the indicated durations and assayed for protein expression (T), ROS content (U), and viability (V). Data are means ± SD [$n = 4$ for (B) and 3 for the rest] and are representative of three independent experiments. *$P < 0.05$, **$P < 0.01$, and ***$P < 0.001$; two-way ANOVA for (C), (D), (L), (O), and (R) and unpaired Student's *t* test for the rest.

biosynthesis. Higher ROS levels activate NRF2 (*31*), leading to suppression of *PIRH2* and stabilization of TAp73. ROS also damage DNA, leading to the activation of the CHK1/2-E2F1 axis and the increase in *TAp73* gene expression. TAp73, in turn, activates G6PD, which stimulates de novo $NADP^+$ production via NADK1 while directly reducing $NADP^+$ to NADPH. Thus, this network enlarges the NADPH pool to restore redox homeostasis (Fig. 8I).

Role of the G6PD-centered redox regulatory network in tumorigenesis

The ability to grow without anchoring to extracellular matrix is a hallmark of the oncogenic state, correlating with tumorigenicity in animals (*49*). We stably knocked down G6PD and its upstream regulators including NRF2, PIRH2, E2F1, and TAp73 individually in PANC-1 using small hairpin RNAs (shRNAs) (Fig. 8J). Knockdown of NRF2 or TAp73 was largely inconsequential for adherent proliferation (Fig. 8K) but detrimental for anchorage-independent growth (Fig. 8L and fig. S7C). Knockdown of E2F1 caused a more severe defect in anchorage-independent growth than that of NRF2 or TAp73 (Fig. 8L and fig. S7C) and also impaired adherent proliferation (Fig. 8K). The latter was expected given the role of E2F1 in cell cycle progression (*50*). Nevertheless, supplementation with NAC partially rescued anchorage-independent growth of E2F1-knockdown cells while having no effect on adherent growth (fig. S7, D to F). Therefore, E2F1 may promote anchorage-independent growth, at least in part, through redox regulation. In contrast to NRF2, TAp73, and E2F1, knockdown of PIRH2 enhanced both adherent proliferation and anchorage-independent growth (Fig. 8, K and L, and fig. S7C).

G6PD knockdown, although minimally affected the adherent proliferation of PANC-1 cells (Fig. 8, J and K), resulted in a stronger effect on anchorage-independent growth than TAp73 or NRF2 knockdown, reducing the number of soft-agar colonies by ~80% (Fig. 8L and fig. S7C). In contrast, forced G6PD expression afforded MIA PaCa-2 cells a stronger ability to grow on adherent plates and in soft-agar medium (Fig. 8, M to O, and fig. S7G). Moreover, supplementation with NAC, which had no notable effect on adherent growth of G6PD-knockdown cells (fig. S7, H and I), almost fully restored the ability of these cells to grow in soft-agar medium (fig. S7, J and K). These results are consistent with the notion that G6PD is a main effector of NRF2 and TAp73 and that its role in anchorage-independent growth is primarily due to redox regulation.

Similarly, depleting NADK1 in PANC-1 cells had a minimal effect on adherent proliferation but noticeably impeded anchorage-independent growth (Fig. 8, P and Q, and fig. S7, L and M). Depleting NADK1 in MIA PaCa-2 cells also had a minor impact on adherent proliferation while markedly reducing anchorage-independent growth (Fig. 8, M to O, and fig. S7G). Thus, NADK1 is required for the maintenance of malignant phenotypes as well. Depleting NADK1 reduced the anchorage-independent growth of G6PD-overexpressing MIA PaCa-2 cells (Fig. 8, M to O, and fig. S7G). Moreover, forced expression of $G6PD^{K171Q}$, the catalytically inactive mutant that retained the ability to stimulate NADK1, enhanced the capability of MIA PaCa-2 cells to grow in soft-agar medium (Fig. 8R). Therefore, the role of G6PD in oncogenic growth is dependent on NADK1.

G6PD supports metastasis

To investigate the function of G6PD in metastasis, we screened for the expression of G6PD and its upstream regulatory components in a panel of pancreatic cancer cell lines with high or low metastatic potentials (*51*, *52*). While NRF2, PIRH2, E2F1, and TAp73 were expressed at variable levels among these cell lines, G6PD was present more abundantly in cell lines with high metastatic potentials (i.e., PANC-1, AsPC-1, and Capan-1) than in those with low metastatic potentials (i.e., MIA PaCa-2 and BxPC-3) (Fig. 8S). Despite their difference, both PANC-1 and MIA PaCa-2 cells up-regulated NRF2, E2F1, and TAp73 and down-regulated PIRH2, following matrix detachment (Fig. 8T), although the former exhibited a stronger ability to withstand oxidative stress and a higher survival rate than the latter when cultured in suspension (Fig. 8, U and V).

To examine the role of G6PD in metastasis, we knocked down endogenous G6PD in PANC-1 cells in which enhanced green fluorescence protein (GFP) was also expressed to facilitate cell detection (PANC-1/GFP). Similar to PANC-1 cells (Fig. 8, J and L), stable knockdown of G6PD by the same shRNA (shRNA #1) markedly reduced the number of soft-agar colonies formed by PANC-1/GFP cells (~80% reduction; Fig. 9, A and B). Similarly, knockdown of G6PD with an independent shRNA (shRNA #2), which decreased G6PD enzyme activity and prevented the increase in NADP(H) pool upon matrix detachment, also reduced colony formation of PANC-1/GFP cells (fig. S8, A to C). These defects caused by G6PD shRNA #2 were rescued by an shRNA-resistant form of G6PD (fig. S8, A to C), indicating the specificity of this shRNA.

To recapitulate the late events of metastasis, including survival in circulation, extravasation from the bloodstream, and metastatic colonization at distant sites, we injected control and G6PD-knockdown PANC-1/GFP cells into athymic nude mice via the tail vein. Control PANC-1/GFP cells formed numerous and relatively large metastases in the lung, but not in the liver, as shown by fluorescence imaging (Fig. 9C and fig. S8D) and hematoxylin and eosin (H&E) staining (Fig. 9, D to F, and fig. S8E). In comparison, G6PD-knockdown PANC-1/GFP cells generated lung metastases that were fewer and far smaller (Fig. 9, C to F). The reduction in metastases was verified by markedly lower levels of GFP in the lung (Fig. 9G and fig. S8F).

An immunohistochemistry (IHC) assay confirmed that lung metastases generated by control PANC-1/GFP cells expressed high levels of G6PD, and small lung metastases generated by G6PD-knockdown PANC-1/GFP cells expressed low levels of G6PD (fig. S8, G and H). Notably, G6PD expression in large tumor nodules generated by G6PD-knockdown cells was comparable to that in the tumor nodules produced by control cells (fig. S8, G and H). Thus, these large tumors in the G6PD-knockdown group likely had escaped G6PD silencing. For comparison, we examined NADK1 expression. NADK1 was present at comparable levels in large and small tumor nodules formed by G6PD-knockdown cells and in tumor nodules formed by control and G6PD-knockdown cells (fig. S8, I and J).

Conversely, we forced G6PD expression in the low-metastatic MIA PaCa-2 cells that were also labeled with GFP (MIA PaCa-2/GFP). G6PD-overexpressing MIA PaCa-2/GFP cells generated 40% more colonies in soft-agar medium compared to control MIA PaCa-2/GFP cells (Fig. 9, H and I). When delivered via tail vein injection, control MIA PaCa-2/GFP formed a limited number of small metastases in the lung (Fig. 9, J to M) but not in the liver (fig. S8, K and L). In comparison, G6PD-overexpressing MIA PaCa-2/GFP cells generated more and larger lung metastases, as indicated by fluorescence imaging (Fig. 9J); H&E staining, which showed a ~25% increase in the number of tumor nodules and a ~120% increase in tumor areas (Fig. 9, K to M); and Western blot, which indicated a ~150% increase in GFP protein levels (Fig. 9N and fig. S8M).

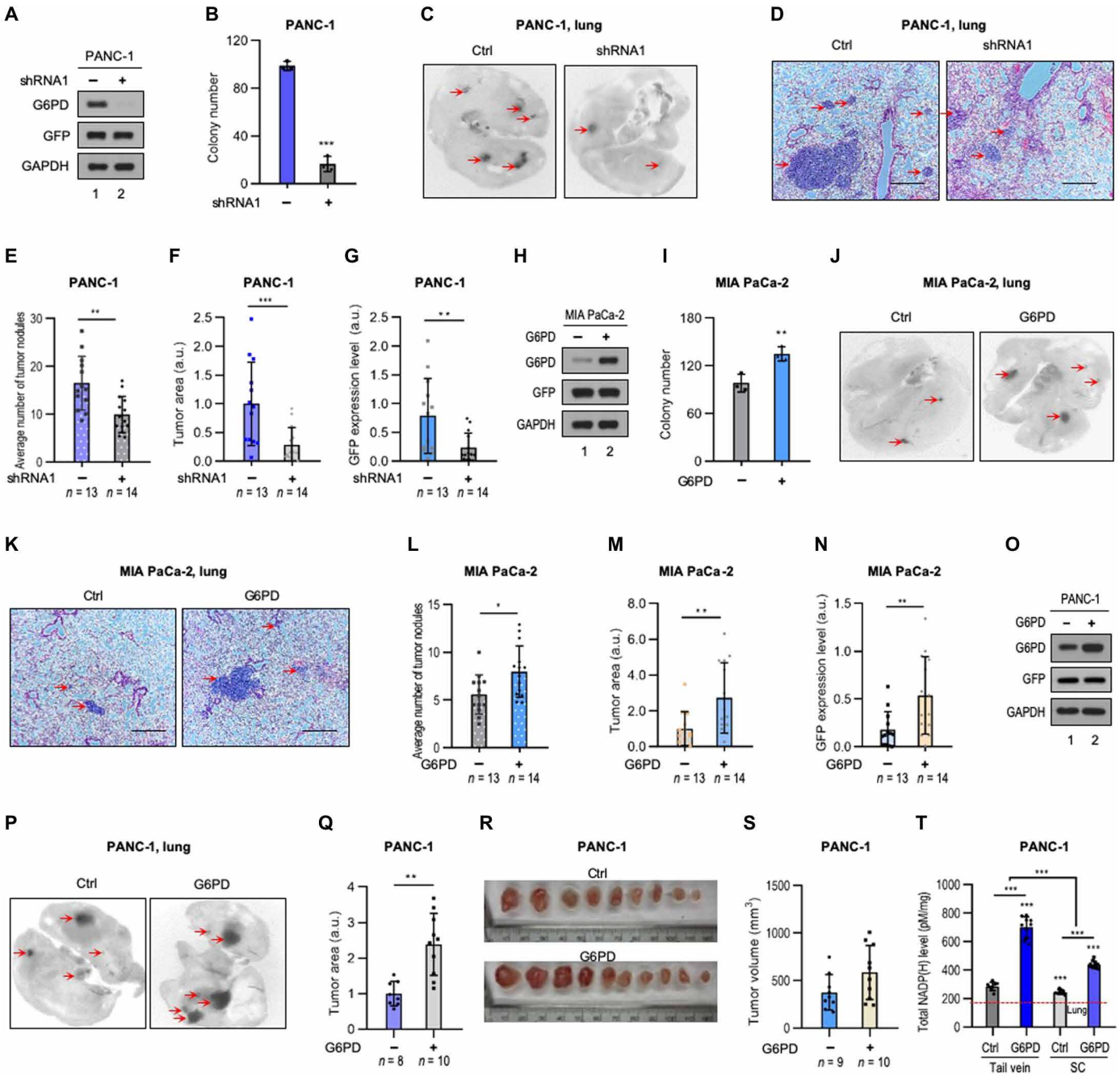

Fig. 9. G6PD promotes metastatic colonization of pancreatic cancer cells. (**A** to **N**) PANC-1/GFP cells with or without G6PD knockdown (A to G) or MIA PaCa-2/GFP cells with or without G6PD overexpression (H to N) were inoculated into immunodeficient mice via tail vein and analyzed for tumor nodules in the lung 8 weeks later. Shown are protein expression in (A and H) and soft-agar colony formation by (B and I) PANC-1/GFP (A and B) and MIA PaCa-2/GFP (H and I) cells, representative GFP images for the lung (C and J), representative tumor images (D and K) and quantification of tumor numbers (E and L) and areas (F and M) by H&E staining, and quantification of GFP expression in the lung by Western blot (normalized by GADPH expression of each sample) (G and N). (G) is related to fig. S8F, and (N) is related to fig. S8M. Red arrows indicate tumors. Scale bars, 450 μm. (**O** to **T**) Control and G6PD-overexpressing PANC-1/GFP cells (O) were inoculated in immunodeficient mice via tail vein (P, Q, and T) or subcutaneous (SC) (R to T) injection, and tumors were analyzed 11 and 10 weeks later, respectively. Show are representative GFP images of lung metastases (P) and quantification of tumor areas based on H&E staining (Q), images (R) and volumes (S) ($P = 0.053$) of subcutaneous tumors, and total NADP(H) levels in lung metastases and subcutaneous tumors (T). Dashed line in (T) indicates the value in normal lung tissue. Data are means ± SD [$n = 3$ for (B) and (I) or as indicated]. $^{**}P < 0.01$ and $^{***}P < 0.001$; two-way ANOVA for (T) and unpaired Student's t test for the rest.

Forced G6PD expression in the highly metastatic PANC-1/GFP cells also bolstered their ability to establish lung metastases in the tail vein injection model (Fig. 9, O to Q). By contrast, G6PD only slightly enhanced the formation of primary tumors by PANC-1/GFP cells in a subcutaneous injection model (Fig. 9, R and S). To investigate the molecular basis underlying this difference, we evaluated the effect of G6PD on the total NADP(H) level in tumors formed by subcutaneous and tail vein injections. Subcutaneous tumors formed by G6PD-overexpressing PANC-1 cells contained an ~80% higher level of total NADP(H) than the corresponding control tumors (Fig. 9T). The difference was wider among lung metastatic tumors, with total NADP(H) levels being ~140% higher in metastases generated by G6PD-overexpressing cells compared to those generated by control cells (Fig. 9T). Collectively, these results indicate that G6PD plays an important role in the formation of primary and especially metastatic tumors. They also suggest that high NADP(H) levels drive cancer metastatic colonization.

Metastasis is generally regarded as a process of migration and invasion of tumor cells. Nevertheless, knockdown of G6PD or NADK1 did not affect the migration or invasion of PANC-1 cells in culture, as shown by wound healing and Matrigel cell invasion assays (fig. S9, A to E). Similarly, treatment with FK866, which blocked de novo $NADP^+$ production (fig. S1L), had no effect on the migration or invasion of PANC-1 cells (fig. S9, F and G), although it effectively prevented the increase in $NADP^+$ and NADPH in, and reduced the viability of, matrix-detached PANC-1 cells (fig. S9, H and I). Therefore, G6PD and NADK1 appear to promote metastasis by enabling the survival, rather than migration and invasion per se, of tumor cells.

Expression of G6PD and its regulators in human tumors

To explore clinical implications of G6PD and its regulators/effector, we analyzed the expression of G6PD, NRF2, PIRH2, E2F1, TAp73, and NADK1 in a tissue microarray (TMA) of primary and metastatic pancreatic tumors. Compared to primary tumors, metastatic tumors expressed substantially higher levels of G6PD, NRF2, E2F1, and TAp73 (Fig. 10, A to D) but noticeably lower levels of PIRH2 (Fig. 10E). However, metastatic and primary tumors expressed similar levels of NADK1 (Fig. 10F), consistent with the notion that NADK1 is mainly regulated at the level of its activity rather than expression. A survey of the public databases revealed that metastatic pancreatic tumors expressed higher levels of G6PD and lower levels of PIRH2 than primary pancreatic tumors (fig. S10, A and B). These results suggest that the G6PD-centered redox regulatory network may be co-opted by metastatic pancreatic cancer.

Consistent with the molecular mechanisms of this redox regulatory network and its role in metastasis, the expression of NRF2 or p73 protein negatively correlated with that of the PIRH2 protein in the pancreatic cancer specimens (Fig. 10, G and H). Moreover, there was a positive correlation between p73 and E2F1 or G6PD expression (Fig. 10, I and J), between NRF2 and p73 or G6PD expression (fig. S10, C and D), and between E2F1 and G6PD expression (fig. S10E). In contrast, PIRH2 expression negatively correlated with G6PD expression (fig. S10F). A survey of a public database (Human Protein Atlas) further confirmed the positive correlation between NRF2 or p73 and G6PD expression in a large cohort of patients with pancreatic cancer (fig. S10, G and H). Moreover, pancreatic cancer patients with high NRF2, E2F1, p73, or G6PD expression had poor survival probability, whereas those with high PIRH2 expression had better survival probability (fig. S10, I to N). These results indicate that G6PD and its regulators may play a critical role in pancreatic cancer progression and metastasis.

DISCUSSION

Role of G6PD and NADK in tumor initiation and metastasis

Tumor cells encounter high oxidative stress during initiation and especially during metastasis. As NADPH provides the ultimate reducing power to virtually all ROS detoxification systems, its levels are a critical determinant for cellular antioxidant capacity. Here, we find that the intracellular NADPH pool is substantially enlarged, along with the $NADP^+$ pool, under matrix detachment and other oxidative stress conditions. This enlargement is mainly due to the metabolic flux through NADK1, but not NADK2. This observation is consistent with the previous findings that NADK1 can protect against oxidative stress (*53*, *54*), while NADK2 may have a primary role in supplying NADP(H) for proline biosynthesis in mitochondria (*55*, *56*).

The level of NADK1 protein does not respond to oxidative stress. Instead, its activity is increased. This increase is mediated by G6PD, which appears to be unique among NADPH-regenerating enzymes for its ability to stimulate NADK1. Although G6PD is a major source of cytoplasmic NADPH (*25*), cells are able to transfer reducing power from the cytosol to mitochondria via mechanisms such as reductive carboxylation of glutamine (*15*). Thus, G6PD may also facilitate redox balance in mitochondria. Notably, forced G6PD expression is able to transform immortalized murine and human cells (*14*, *57*), an extraordinary property among metabolic enzymes. This property emphasizes the importance of its metabolic consequences in tumor initiation. We recently showed that these metabolic consequences are the up-regulation of antioxidant defense capacity and nucleotide precursor availability, which are themselves sufficient to transform immortalized cells (*14*). This unexpected finding reveals basic elements of oncogenic transformation. In addition, it indicates that metabolic reprogramming per se can be a transforming event.

Up-regulation of G6PD is also associated with metastasis of breast cancer and melanoma (*16*, *17*, *58*). Thus, G6PD-directed metabolic consequences may also promote tumor progression. Nevertheless, the role of G6PD in cancer cells has been attributed mainly to NADPH regeneration and ribose production. Here, we show that an important function of G6PD is probably the direct activation of NADK1 for de novo $NADP^+$ biosynthesis. Notably, among various observations that support this notion, we find that $G6PD^{K171Q}$, which is able to activate NADK1 but not regenerate NADPH, is still highly effective in ameliorating oxidative stress and promoting oncogenic growth (Fig. 8R).

The activity of NADK1 can also be stimulated by AKT- and PKC-mediated phosphorylation (*35*, *36*), further highlighting NADK1 as a focal point of redox regulation. Nevertheless, AKT is inhibited in matrix-detached cells due to decreased epidermal growth factor receptor signaling (*7*) and may not contribute to NADK1 activation in these cells. Furthermore, we find that in the absence of G6PD, tumor cells cannot accentuate the NADK1 flux or activate NADK1 in the face of redox stress (Fig. 2G and fig. S3, F to H). Given that a rise in $NADP^+$ levels, even transiently, can have detrimental consequences by interfering with other essential metabolic pathways such as folate metabolism (*21*), G6PD-mediated NADK1 activation offers a unique advantage as a redox-regulatory mechanism. It couples $NADP^+$ production and reduction both temporally and spatially, so that extra $NADP^+$ is only produced when and where it can be

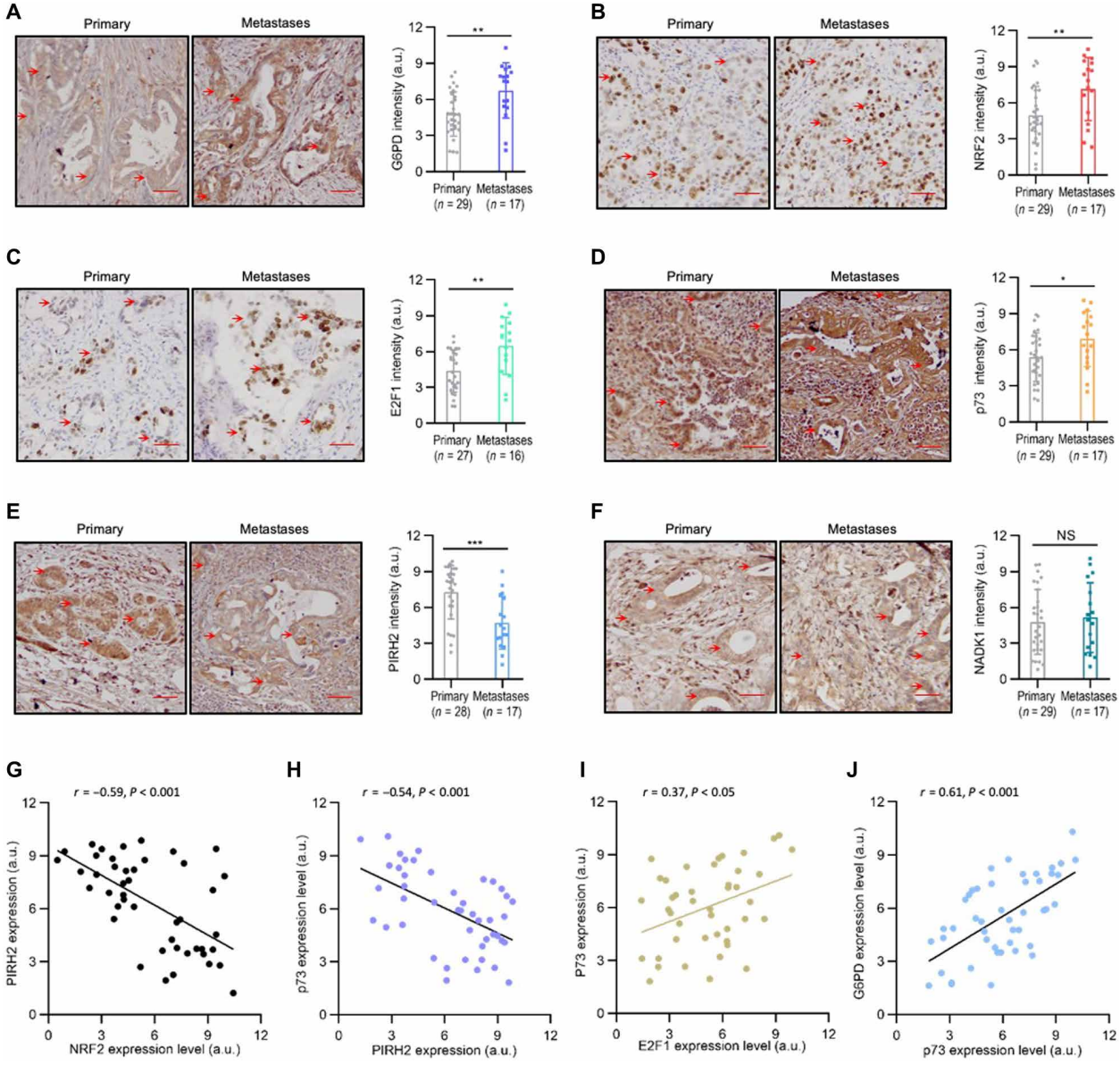

Fig. 10. Expression of G6PD and its regulators in primary and metastatic pancreatic cancers. (**A** to **F**) TMAs containing primary and metastatic pancreatic tumors were analyzed by IHC for expression of G6PD (A), NRF2 (B), E2F1 (C), p73 (D), PIRH2 (E), and NADK1 (F). The representative image of IHC staining (left) and intensity of antibody staining (a.u.) (right) are shown. Scale bars, 60 μm. (**G** to **J**) Correlation coefficient analysis for the expression of NRF2 (a.u., same below) and PIRH2 ($n = 45$) (G), PIRH2 and p73 ($n = 45$) (H), E2F1 and p73 ($n = 43$) (I), and p73 and G6PD ($n = 46$) (J). The r and P values of Pearson correlation coefficient are shown. Data are means ± SD (n as indicated). *$P < 0.05$, **$P < 0.01$, and ***$P < 0.001$; unpaired Student's t test.

effectively reduced to NADPH. The role of G6PD in NADK1 activation may also provide an explanation for the long-standing, perplexing observation that although G6PD normally runs far below its maximal capacity (*33*, *34*), it is still markedly up-regulated under various stress conditions.

A cellular network for maintaining redox homeostasis

The G6PD-NADK1 connection in redox regulation emphasizes the importance of the mechanism that governs G6PD expression. Here, we show that TAp73 is a redox-responsive proximal transcription factor of *G6PD*. TAp73 is a major isoform class of the p53-reglated protein p73, containing an intact N-terminal TA domain (*59*, *60*). In contrast to the other major isoform that lacks this domain (ΔNp73), which functions as an oncogene by exerting a dominant-negative effect on p53, the role of TAp73 in tumorigenesis is more complex. As opposed to p53, which is the single most frequently mutated gene in cancer, TAp73 is rarely mutated and instead is often overexpressed in cancer (*59*, *60*). Our previous studies showed that TAp73 promotes cell proliferation through the activation of G6PD (*41*, *42*), as well as phosphofructokinase-1, liver type, catalyzes a rate-limiting step in glycolysis (*61*). Extending from these findings, we show here that TAp73 itself is highly responsive to oxidative stress, providing a crucial link between oxidative stress and enzymes that participate in glucose metabolism and ROS detoxification.

TAp73 itself is regulated by at least two redox response pathways. TAp73 is activated at posttranslational level by the NRF2-PIRH2 axis. As a principal regulator of cellular redox homoeostasis, NRF2 is normally kept at low levels due to Kelch-like ECH-associating protein 1 (Keap1)–mediated ubiquitination and degradation (*31*). Oxidative or electrophilic molecules react with key cysteine residues on Keap1, leading to Keap1 inactivation and NRF2 accumulation. NRF2 then regulates the expression of hundreds of genes, many of which, similar to G6PD, are involved in ROS detoxification (*32*). However, in contrast to a common notion (*32*), we find that NRF2 does not directly stimulate G6PD expression. Among the various factors that are implicated in TAp73 regulation, NRF2 suppresses the expression of the E3 ligase PIRH2, thereby prolonging the half-life of the TAp73 protein. Despite this indirect effect, G6PD is likely a major target of NRF2 for redox regulation. Elevating G6PD expression, even to a moderate extent, can strongly bolster antioxidant defense despite a reduction in the other NRF2 target genes, while knocking down G6PD leads to a severe defect in redox regulation despite an increase in the other NRF2 targets (Fig. 5, M to P). Consistent with this notion, a recent study showed that G6PD loss suppresses growth of tumors in which the NRF2 antioxidant program becomes constitutively active (*62*).

TAp73 is also regulated at transcriptional level by the CHK1/2-E2F1 axis under redox stress conditions. The E2F family of transcriptional factors are central regulators of cell cycle progression, acting downstream of cyclin-dependent kinases and retinoblastoma protein (RB) (*50*). E2F1 also functions in DNA damage response. It is activated by CHK1 and CHK2. In turn, E2F1 stimulates *p73* expression to induce apoptosis (*48*). Although ROS can modify nucleotide bases such as oxidation of guanine to form 8-oxo-7,8-dihydroguanine, activation of DNA damage response under oxidative stress conditions is less appreciated. By revealing the activation of the CHK1/2-E2F1-TAp73 pathway under various redox stress conditions, our results suggest that DNA damage signaling may be an integral part of the cellular mechanism that maintains redox homeostasis. Moreover, early studies showed that DNA damage signaling presents a barrier to oncogenic transformation, but what causes DNA damage in early tumorigenesis is not well defined (*63*, *64*). As oxidative stress is commonly encountered by premalignant cells, it is likely a cause for DNA damage in these cells.

Unlike conditions of severe DNA damage, the activation of TAp73 following matrix detachment is proapoptotic (*48*). Thus, the outcome of TAp73 activation may be context dependent, perhaps also influenced by amplitude and duration of the activation. Recently, studies showed that E2F1 protects cells from oxidative stress, and E2F1 inactivation leads to hypersensitivity to oxidant treatment (*65*, *66*). The ability of E2F1 to stimulate G6PD via TAp73 likely provides a molecular basis for this observation. E2F1 may also engage the TAp73-G6PD axis in other cellular settings. For example, E2F1 regulates TAp73 expression in a cell cycle–dependent manner (*67*). Thus, E2F1 may increase the supply of NADPH and ribose through the TAp73-G6PD connection, coordinating nucleotide synthesis with cell cycle progression. Moreover, a previous study showed that G6PD is activated by mitogenic signals through an unknown mechanism (*68*). Because E2F1 is stimulated by mitogenic signals, it may link mitogenic signals with G6PD to support cell proliferation.

In summary, the current study reveals that G6PD-mediated expansion of the total NADP(H) pool is a crucial component of the antioxidant defense associated with oncogenic growth and metastasis. It defines a cellular network that activates G6PD, thereby permitting simultaneous up-regulation of $NADP^+$ biosynthesis and its reduction to NADPH. NADPH is a central metabolite involved in many other cellular events besides redox balance and biosynthesis, including, for example, circadian rhythms (*69*). Via NADK, NADPH is also closely associated with NAD^+, which plays a broad role in cell physiology (*70*). Therefore, the mechanisms defined here that regulate $NADP^+$ production and reduction may influence a wide range of processes in normal and malignant cells.

MATERIALS AND METHODS

Antibody and reagents

Antibodies against the following proteins/epitopes were purchased from the indicated sources: Akt (pan), G6PD (Western blot), 6PGD, IDH1, Itch, NADK1 (Western blot and IP), NRF1, NRF2 (Western blot and ChIP), p-Akt (S473), p-Chk1 (S345), p-PKC (pan) (βII S660), phospho-Akt substrate motif (RRXpS/pT), phospho-PKC substrate motif [R/KXpSX(R/K)], p300, p73 (Western blot), hemagglutinin (HA) tag, Flag tag, GFP, SUMO-1, mouse immunoglobulin G (IgG), horseradish peroxidase (HRP) mouse IgG, rabbit IgG (ChIP and IP), and HRP rabbit IgG (Cell Signaling Technology, Beverly, MA); β-actin, c-Abl, p-c-Abl (Y412), p53, PKC, c-Jun, E2F1 (Western blot and IHC), NAMPT [pre-B-cell colony-enhancing factor 1 (PBEF1)], NMNAT1, MDM2, ME1, PML, Trim32, and glyceraldehyde-3-phosphate dehydrogenase (GAPDH) (for human and mouse) (Santa Cruz Biotechnology, Dallas, TX); IDH2 and NADK2 (Abcam, Cambridge, MA); ALDH1L2, G6PD (IHC), NADK1 (IHC), and PIRH2 (Western blot and IHC) (Proteintech, Rosemont, IL); NEDL2, NRF2 (IHC), and p73 (IHC) (Thermo Fisher Scientific, Waltham, MA); biotinylated anti-mouse IgG (IHC) and biotinylated anti-mouse IgG (IHC) (Vector Laboratories, Burlingame, CA); ME2 and p-histone H2A.X (pγ-H2AX S139) (Sigma-Aldrich, St. Louis, MO); and ALDH1L1 (LifeSpan Biosciences, Seattle, WA).

The following reagents were purchased from Sigma-Aldrich (St. Louis, MO): NAM-2,6,7-$^{13}C_3$-(pyridyl-^{15}N) ($^{13}C_3$-^{15}N-NAM), (−)-riboflavin, thiamine pyrophosphate, sodium pyruvate solution, adenosine triphosphate (ATP) magnesium salt, glucose 6-phosphate, bovine serum albumin (BSA), dialyzed fetal bovine serum (FBS), FBS, poly(2-hydroxyethyl methacrylate) (poly-HEMA), NAC, β-NAD^+, paraformaldehyde (PFA), crystal violet, 2′,7′-dichlorofluorescin diacetate (DCFDA), 3× FLAG peptide, anti-FLAG M2 Affinity Gel, ammonium bicarbonate (NH_4HCO_3, for LC-HRMS), 6xHis-NADK1 protein (human, purified from *Escherichia coli*), G6PD protein (human, purified from *E. coli*), CHX, MG132, diamide, EDTA, *N*-ethylmaleimide (NEM), SDS, disuccinimidyl suberate (DSS), Triton X-100, tris-HCl, propidium iodide (PI), and protease inhibitor cocktail. Glucose solution (20%, cell culture), Hepes, hydrogen peroxide (H_2O_2) solution, T4 ligase, Pierce anti-HA magnetic beads, trypan blue solution, ribonuclease inhibitor, and NP-40 were purchased from Thermo Fisher Scientific. Restriction enzymes—BsmBI, DpnI, NheI-HF, HindIII-HF, XbaI, AgeI-HF, EcoRI-HF, and XhoI—were purchased from New England Biolabs (Ipswich, MA). Acetonitrile, formic acid, and water for LC-HRMS were purchased from EMD Millipore (Burlington, MA). The following reagents were purchased from the indicated sources: human recombinant epidermal growth factor (rEGF) (STEMCELL Technologies, Cambridge, MA); FK866 hydrochloride (Tocris Bioscience, Minneapolis, MN); MK-2206 (Selleck Chemicals); G6PD inhibitor (G6PDi-1), phorbol

12-myristate 13-acetate, and gallotannin (Cayman Chemical, Ann Arbor, MI); protein A/G agarose beads (Santa Cruz Biotechnology); low-temperature melting agarose and MEGM BulletKit Growth Media (Lonza, Basel, Switzerland); folic acid (MP Biomedicals, Solon, OH); Dulbecco's modified Eagle's medium (DMEM) Base (without L-glutamine, L-cystine, glucose, phenol red, and sodium pyruvate) (United States Biological, Salem, MA); 4,6-diamidino-2-phenylindole (Vector Laboratories, Burlingame, CA); Dako Dual Endogenous Enzyme Block (DAKO, Little Ferry, NJ); and Novocastra Epitope Retrieval Solutions (Leica Biosystems, Buffalo Grove, IL).

siRNAs for NRF2, PIRH2, p73, G6PD, and IDH1 were purchased from Thermo Fisher Scientific; siRNA for NADK1, E2F1, and ALDH1L2 was purchased from Santa Cruz Biotechnology; and siRNA for NADK2 was purchased from Horizon Discovery (St. Louis, MO). Primers for quantitative real-time polymerase chain reaction (PCR) are listed in table S2 and were purchased from Integrated DNA Technologies (Coralville, IA).

Plasmids

pRK5-HA-TAp73α and pRK5-Flag-TAp73α were constructed by amplifying the open reading frame of TAp73α from pBabe-TAp73α with primers (forward, 5′ TCCTCTAGAATGGCCCAGTCCAC-CGCC 3′; reverse, 5′ TCCAAGCTTTCAGTGGATCTCGGCCTCC 3′) and cloned it into pRK5-HA and pRK5-Flag, respectively, using restriction sites Xba I and Hind III. pRK5-Flag-NADK1, pRK5-Flag-G6PD, pRK5-Flag-G6PD^{K171Q}, pBABE-G6PD, pBABE-G6PD^{K171Q}, and pBABE-TAp73α vectors were previously described (*14*, *41*). pcDNA3.1-Flag-ALDH1L2 and pcDNA3.1-Flag-PIRH2 vectors were purchased from GenScript (Piscataway, NJ). pcDNA3.1-Flag-IDH1 (#62906), pRK5-HA-ubiquitin (#17605), and pCMV-VSV-G (#8454) vectors were purchased from Addgene (Watertown, MA). NRF1 and NRF2 pLX304 vectors were purchased from the High-throughput Screening Core at the University of Pennsylvania (Philadelphia, PA). pLenti-GFP vector was purchased from Cell Biolabs (San Diego, CA). pReceiver-Lv105-G6PD vector was purchased from GeneCopoeia (Rockville, MD). pCL-Ampho vector was purchased from Novus Biologicals (Littleton, CO).

shRNAs for PIRH2, NADK1, and E2F1 were purchased from the High-throughput Screening Core at the University of Pennsylvania (Philadelphia, PA); shRNA for NRF2 was purchased from Santa Cruz Biotechnology; G6PD shRNA #1 and TAp73 shRNA were described previously (*30*, *41*). G6PD shRNA #2 was generated in vector by inserting in pLKO.1 an shRNA hairpin, which targets the 3′ untranslated regions of G6PD mRNA, using Age I and Eco RI restriction sites. The target sequence of G6PD shRNA #2 is 5′ GCCTCTCT-GCTATAAGAAA 3′.

CRISPR-CAS9 knockout vectors for NADK1 were cloned by inserting the guide sgRNA sequences to the lentiGuide-pour vector by Bsm BI restriction enzyme. The guide sequences are 5′ CAGCT-GTTGTTCTCCGGAGT 3′ (sgRNA1) and 5′ TCTGTACCTTTC-GAGAAGGT 3′ (sgRNA2).

Cell culture, transfection, and infection

Human embryonic kidney (HEK) 293T, pancreatic cancer cells AsPC-1, BxPC-3, Capan-1, MIA PaCa-2, and PANC-1 cells were cultured in DMEM (Thermo Fisher Scientific, Waltham, MA); human mammary epithelial cells (HMECs) were cultured in MEGM BulletKit Growth Media (Lonza, Basel, Switzerland); human hepatocellular carcinoma HepG2 cells were cultured in Eagle's Minimum Essential Medium (EMEM) (Thermo Fisher Scientific); human colorectal carcinoma HCT116 and human osteosarcoma U2OS cells were cultured in McCoy's 5A serum-free medium (Sigma-Aldrich); and human prostate cancer PC-3 cells were cultured in RPMI 1640 medium (Thermo Fisher Scientific), with each medium supplemented with 10% FBS (Sigma-Aldrich, Allentown, PA). Cells were maintained at 37°C in a humidified incubator with 5% CO_2.

For matrix-detached culture, plates were precoated with 1.2% poly-HEMA (w/v) (dissolved in 95% ethanol in water solution). Cells were seeded at the same density for matrix-attached and matrix-detached conditions. When indicated, cells were treated with 1 mM NAC or 50 μM H_2O_2.

DNA plasmid transfection, retroviral/lentiviral vector packing in HEK293T cells, and viral transduction of target cells were performed as described previously (*14*). Lipofectamine RNAiMAX (Thermo Fisher Scientific) was used to transfect siRNAs following the manufacturer's instruction. For siRNA knockdown, cells were treated with siRNA 12 hours after seeding and treated with indicated agents or cultured under matrix-attached or matrix-detached condition, 24 hours after siRNA transfection.

Western blot and quantitative real-time PCR

Whole-cell lysates were prepared in radioimmunoprecipitation assay (RIPA) buffer [1% Triton X-100, 1% sodium deoxycholate, 0.1% SDS, 150 mM NaCl, 10 mM tris-HCl (pH 7.5), 5 mM EDTA, and 1× protease inhibitor cocktail]. For GFP expression in lung tumor nodules, one-third of the lung of each mouse was homolyzed with nitrogen and mortar and lysed with 1 ml of RIPA buffer with protease inhibitor cocktail immediately. Equivalent amounts of protein were separated by SDS–polyacrylamide gel electrophoresis (PAGE) and transferred to a polyvinylidene difluoride membrane (Millipore). Proteins were detected using an enhanced chemiluminescence system (Amersham Biosciences, Piscataway, NJ, USA).

Total RNA was extracted with TRIzol (Invitrogen) following the manufacturer's protocol. RNA (2 μg) was reverse-transcribed by the High Capacity cDNA Reverse Transcription Kit (Applied Biosystems). Quantitative real-time PCR was performed using SYBR Green PCR Master Mix in the 7900HT Fast Real-Time PCR System (Applied Biosystems). GAPDH or β-actin was used as an endogenous reference gene. The primer sequences for real-time PCR are listed in table S2.

Immunoprecipitation

HEK293T cells were treated with MG132 for 12 hours before being lysed in the IP lysis buffer [50 mM Hepes (pH 7.4), 150 mM NaCl, 1.5 mM $MgCl_2$, 4 μM MG132, 10% glycerol, 0.5% NP-40, 0.5% Triton X-100, and 1× protease inhibitor cocktail] by gentle sonication. Cell lysates were immunoprecipitated with anti-FLAG M2 magnetic beads or anti-HA magnetic beads as indicated. Immunoprecipitated proteins and cell lysates were separated by SDS-PAGE, followed by Western blot.

Protein purification

Flag-NADK1 was transfected into PANC-1 cells via Lipofectamin 2000–mediated gene transfer. Forty-eight hours later, cells were cultured under matrix-attached or matrix-detached conditions for another 12 hours before being harvested using a buffer [20 mM tris-HCl (pH 7.4), 150 mM NaCl, 0.5% Triton X-100, 0.5% NP-40, and 10% glycerol]. Flag-NADK1 was purified as described (*14*). Protein concentration was determined by SDS-PAGE and Coomassie blue staining, along with a protein standard (BSA).

Cross-linking

For protein cross-linking, HEK293T cells were treated with or without G6PD inhibitor (60 μM) for 24 hours. Cells were collected and treated with control (0 mM) or different concentrations (1 and 2 mM) of DSS on ice for 45 min and then lysed with RIPA buffer and analyzed by Western blot. Endogenous p53 was used as a control for cross-linking.

In vivo ubiquitination

Flag-TAp73 and HA-ubiquitin were expressed in HEK293T cells that were pretreated with or without NRF2 and/or PIRH2 siRNAs. Cells were treated with MG132 for 6 hours and lysed in 1% SDS. After boiling for 15 min, lysates were diluted 10 times with cold lysis buffer supplemented with 1× protease inhibitor cocktail and 10 mM NEM. After incubation with the indicated antibodies, immunoprecipitates were analyzed by Western blot.

ROS quantification

ROS were quantified as previously described (*14*). Briefly, cells were pretreated with 10 mM DCFDA (2′,7′-dichlorodihydrofluorescein) for half an hour before being collected for the assays. After washing twice with phosphate-buffered saline (PBS), cells were stained with PI for 2 min and then analyzed by a BD Accuri C6 flow cytometer (BD Biosciences, San Jose, CA) immediately. The DCFDA signals were determined after excluding PI-positive–stained cells (dead cells). Relative ROS level is normalized by that of control cells (or treatment control) under matrix-attached conditions.

Cell viability

Cells treated with siRNAs, NAC, or H_2O_2 were cultured under matrix-attached or matrix-detached conditions for the indicated time. Cells were harvested and stained with an Annexin V/PI kit following the manufacturer's protocol. Cells without Annexin V and PI staining, Annexin V (−) and PI (−), were characterized as viable cells. The ratio of viable cells was determined by a BD Accuri C6 flow cytometer and normalized with that of control cells under matrix-attached condition without any treatment.

Cell proliferation and BrdU incorporation

Cell number was determined by a Cell Counting Kit-8 (CCK-8) (Sigma-Aldrich) following the manufacturer's protocol. Relative cell number was normalized by the number of viable cells on day 0. BrdU (5-bromo-2′-deoxyuridine) incorporation was determined by a BrdU Cell Proliferation Assay Kit (BioVision, Milpitas, California) following the manufacturer's protocol. BrdU incorporation rate was normalized by the cell number measured by a CCK-8 kit. Relative BrdU incorporation rate was normalized by that of control cells under matrix-attached condition.

Cell migration and invasion

Cell migration was determined by a wound healing assay. Briefly, cells with or without siRNA treatment were cultured in 10-cm dishes. When cell confluence reached 90 to 100%, "wound gaps" of about 400 μm in a cell monolayer were created by scratching, captured by a microscope, and recorded. After 16 hours of incubation, the wound gaps were again captured and recorded. The differences of initial and final wound gaps were measured to determine cell migration rate.

Cell invasion was determined by a Corning BioCoat Matrigel Cell Invasion Assay (Corning, Tewksbury, MA, USA) following the manufacturer's instruction. Briefly, cells with or without siRNA treatment were cultured in FBS-free DMEM (Thermo Fisher Scientific) for 4 hours. Cells were then digested and resuspended. Cells (~40,000) in 0.5 ml were added to the 24-well invasion chamber (pore size, 8 μm) precoated with Corning Matrigel matrix (Corning). The invasion chamber was incubated for 24 hours with 10% FBS DMEM as a chemoattractant (0.75 ml) in the bottom wells in a normal cell culture incubator. Cells that invaded into the lower chamber were stained with 1% crystal violet and captured by a microscope for quantification.

Soft-agar colony formation

Pancreatic cancer cells were seeded in the top layer of 0.36% soft agar premixed with culture medium (supplemented with 10% FBS) in six-well plates (500 cells per well for PANC-1 cells and 800 cells per well for MIA Paca-2 cells). Cells were incubated at 37°C for 2 weeks. For treatment, cells were supplemented with NAC (1 mM) or H_2O_2 (50 μM) mixed in the top and bottom soft-agar medium. The 0.36% soft-agar medium with or without the indicated treatments was replenished on the top once a week. By the end of the experiment, the colonies were stained with 0.05% crystal violet (dissolved in a 4% PFA solution) for imaging and quantification by ImageJ (National Institutes of Health).

G6PD, NAMPT, NMNAT1, and NADK1 enzyme activity

G6PD enzymatic activity was determined by the Glucose 6 Phosphate Dehydrogenase Activity Fluorometric Assay Kit (Abcam) following the manufacturer's protocols. Enzymatic activities were normalized by the total amount of proteins, which was determined by a Bio-Rad protein assay kit (Bio-Rad, Hercules, CA).

NAMPT and NMNAT1 enzymatic activities were determined by the NAMPT Activity Colorimetric Assay Kit (Abcam) and the NMNAT1 Activity Colorimetric Assay Kit (Abcam), respectively, following the manufacturer's protocols. Briefly, the enzymes were immunoprecipitated from cell lysates, washed, and analyzed by the two-step methods. The input of the assays was analyzed by Western blot.

NADK1 activity was assayed as described (*14*) with modifications. Approximately 0.5 μg of purified Flag-NADK1 from PANC-1 under matrix-attached or matrix-detached conditions was subjected to the assay that coupled NADK-mediated production of $NADP^+$ from NAD^+ with G6PD-mediated reduction of $NADP^+$ to NADPH, which was measured as a change in absorbance at 340 nm over time. Measurements of 0.5 μg of NADK1 enzymatic velocity at 2 mM NAD^+ were performed in a 100-μl reaction mixture containing 10 mM ATP, 10 mM glucose-6-phosphate, 1 μg of human G6PD purified from *E. coli* (Sigma-Aldrich), 10 mM $MgCl_2$, and 100 mM tris-HCl (pH 8.0). Optical density at 340 nm was measured at 37°C every 3 min over the course of 30 min.

Quantification $NADP^+$ and NADPH levels and NADPH/$NADP^+$ ratio by colorimetric assay

The total cellular $NADP^+$ and NADPH levels were determined by an NADP/NADPH quantitation colorimetric assay kit with an NADPH standard (BioVision Inc., San Francisco, CA) and normalized by the total protein of each sample. To determine the NADPH/$NADP^+$ ratio, an NADP/NADPH-Glo assay kit (Promega, Madison, WI) was also used, following the manufacturers' protocol. The relative NADPH/$NADP^+$ ratio was normalized by that of control cells (or treatment control) under matrix-attached condition.

Glucose uptake, glutamine uptake, and lactate secretion

Glucose uptake and glutamine uptake were determined by a Glucose Colorimetric/Fluorometric Assay Kit (Sigma-Aldrich) and a Glutamine and Glutamate Determination kit (Sigma-Aldrich), respectively, following the manufacturer's protocols. Briefly, cells with or without siRNA treatment were cultured in DMEM (Thermo Fisher Scientific) supplemented with 10% dialyzed FBS (Sigma-Aldrich) under matrix-attached or matrix-detached conditions for 6 hours. The medium conditioned with or without cells was collected and assayed for glucose and glutamine concentrations to determine glucose uptake and glutamine uptake. Glucose and glutamine uptake per hour were normalized by the total protein of each sample. Lactate secretion was determined by a Lactate Assay Kit (Sigma-Aldrich) following the manufacturer's protocol. Briefly, the conditioned medium collected above for glucose uptake and glutamine uptake assays was also assayed for lactate secretion. The lactate secretion per hour was normalized by the total protein of each sample. Glucose uptake rate potential for aerobic oxidation (J) was calculated from glucose uptake rate (E) and lactate secretion rate (F) of the same sample based on the formula $J = E - \frac{1}{2}F$

Global metabolomic analysis

Metabolite analysis was performed as previously described (*71*). Cells were washed twice with ice-cold 1× PBS, immediately covered with −20°C solvent A (40:40:20 methanol:acetonitrile:water with 0.1 M formic acid solution, precooled on ice) for the extraction of metabolites, and scraped down. The mixtures were collected in a microcentrifuge tube and incubated on dry ice for 5 min. The volume of the extraction solution (in microliters) was 50× of the cell volume in packed cell volume. Solvent B [15% (w/v) NH_4HCO_3 in water solution] was added to solvent A in a ratio of 8.8 μl of solvent B per 100 μl of solvent A and mixed, followed by centrifugation at 16,000*g* at 4°C for 15 min. The supernatant was transferred to LC-MS autosampler vials for analysis. Briefly, a quadrupole orbitrap mass spectrometer (Q Exactive Plus, Thermo Fisher Scientific) operating in negative ion mode was coupled to hydrophilic interaction chromatography via electrospray ionization and used to scan from mass/charge ratio 73 to 1000 at 1 Hz and 140,000 resolution. LC separation was achieved on a XBridge BEH Amide column (2.1 mm by 150 mm, 2.5-μm particle size, 130-Å pore size; Waters) using a gradient of solvent A [20 mM ammonium acetate and 20 mM ammonium hydroxide in 95:5 water:acetonitrile (pH 9.45)] and solvent B (acetonitrile). Flow rate was 150 μl/min. The gradient was as follows: 0 min, 85% B; 2 min, 85% B; 3 min, 80% B; 5 min, 80% B; 6 min, 75% B; 7 min, 75% B; 8 min, 70% B; 9 min, 70% B; 10 min, 50% B; 12 min, 50% B; 13 min, 25% B; 16 min, 25% B; 18 min, 0% B; 23 min, 0% B; 24 min, 85% B; and 30 min, 85% B. Data were analyzed using the MAVEN software35. Metabolite levels were normalized by the total protein of each sample extracted by RIPA buffer.

Quantification of NADPH by LC-MS

NADPH was also measured by LC-MS as previously described (*72*). For matrix-attached conditions, cells were seeded in standard six-well plates and cultured in DMEM with 10% dialyzed FBS for the indicated time. Medium was aspirated, and metabolites were extracted with 600 μl of solvent A (40:40:20 methanol:acetonitrile:water with 0.1 M formic acid solution, precooled on ice). After 30 s, extraction was quenched with 75 μl of solvent B [15% (w/v) NH_4HCO_3 in water solution]. For matrix-detached conditions, cells were seeded in poly-HEMA–precoated six-well plates and cultured in the same medium as above for the indicated time. Upon harvesting, cells were gently collected into 1.5-ml Eppendorf tubes by pipetting and centrifuged at 1000*g* for ~30 s. The medium was aspirated, and cell pellets were extracted with 200 μl of solvent A. After 30 s, extracts were quenched with 25 μl of solvent B. For both conditions, total time from cell collection to extract quenching was ~1 min to minimize disturbance of cell metabolism. Samples were then incubated at −80°C for 30 min, followed by centrifugation at ~16,000*g* and 4°C to remove insoluble cell components. The resulting supernatants were analyzed directly by LC-MS. Metabolites were analyzed using a quadrupole orbitrap mass spectrometer (Q Exactive Plus, Thermo Fisher Scientific) operating in negative ion mode, coupled via electronspray ionization to hydrophilic interaction chromatography with LC separation on a XBridge BEH Amide column. Metabolite abundances were normalized to extraction dilution and packed cell volumes for each condition. Data were analyzed using the MAVEN software suite (*73*).

Metabolic flux to NAD^+ and $NADP^+$

[$^{13}C_3$-^{15}N]-NAM ($^{13}C_3$-^{15}N-NAM) was used to determine the metabolic flux to NAD^+ and $NADP^+$ flux as described previously (*35*, *39*). Briefly, cells were treated with control siRNA or siRNA against G6PD or NADK1 for 24 hours in DMEM with 10% dialyzed FBS. Cells will then be cultured under matrix-attached or matrix-detached condition for 9 hours with NAM-free DMEM and incubated with the same medium containing $^{13}C_3$-^{15}N-NAM (4 mg/liter) and 10% dialyzed FBS for another 3 hours. The NAM-free medium was prepared using powdered DMEM supplemented with standard DMEM concentrations of folic acid, niacinamide, pyridoxal, riboflavin, thiamine, glucose, sodium pyruvate, and, in the place of NAM, $^{13}C_3$-^{15}N-NAM, with pH adjusted to 7.2. The metabolites were collected and immediately analyzed by LC-MS to determine the ratio of labeling.

Oxygen consumption

Oxygen consumption rate was measured with an Extracellular Oxygen Consumption Assay Kit (Abcam, Cambridge, MA) according to the manufacturer's protocol. Cells with or without siRNA treatment were cultured in 150 μl of prewarmed DMEM (Thermo Fisher Scientific) supplemented with 10% FBS (Sigma-Aldrich) under matrix-attached or matrix-detached conditions for 6 hours. Before the assay, 10 μl of phosphorescent oxygen probe was added to each well and mixed. The medium was then immediately sealed with prewarmed high-sensitivity mineral oil. Fluorescence was measured every 2.5 min at 37°C for 2 hours by BioTek Synergy HT1 (BioTek, Winooski, VT).

Chromatin immunoprecipitation

To identify putative response elements (REs) of transcriptional factor NRF2, the promoter region of the PIRH2 gene was analyzed with the Eukaryotic Promoter Database (Swiss Institute of Bioinformatics, Lausanne, Switzerland; software, http://epd.vital-it.ch/). For ChIP assays, cells were cross-linked with 1% formaldehyde for 15 min at room temperature. The cross-linking was stopped by the addition of 100 mM tris-HCl (pH 9.4). Cell lysates were sonicated to generate DNA fragments with an average size below 1000 base pairs (bp) and immunoprecipitated with NRF2 antibody. Bound DNA fragments were eluted and amplified by quantitative real-time PCR. Primer pairs

for putative AREs are listed as follows: ARE1, 5′ GGCTTGTACATTTTCCTTCCACC 3′ and 5′ AGCAGCTCTGACAATCTGAGT 3′; ARE2, 5′ GGGGCTGCGAGCACTATG 3′ and 5′ ATCCAAGCCTAACCACCTGCC 3′; ARE3, 5′ TTTTTGGCAAGGCGATAAGCC 3′ and 5′ CTTCGGCAGCAAAAGACGAAT 3′. The relative enrichment folder was calculated by normalizing with the IgG controls.

Luciferase reporter assay

The PIRH2 promoter region of a 1295-bp DNA fragment (−948 to +300) containing all three putative AREs for NRF2 (ARE1, −847; ARE2, +77; and ARE3, +324) was cloned into the pGL3-basic firefly luciferase reporter vector (Promega, Madison, WI, USA) at restriction sites Nhe I and Xhol. Primers to amplify the DNA fragment by PCR were 5′ CACGCTAGCGCTGTGTACCCCGAGTATGA 3′ and 5′ GACTCGAGGAGACCACTGTGCAAGCCTA 3′. The PIRH2 promoter region with the same 1295-bp DNA fragment (−948 to +300), except for a mutation on putative ARE3 as indicated, was also cloned into the pGL-3 basic firefly luciferase vector using the same restriction sites. Primers to amplify the DNA fragment by PCR were 5′ CACGCTAGCGCTGTGTACCCCGAGTATGA 3′ and 5′ GACTCGAGGAGACCACTGTGCAATACTAAAATCTTCCCAAGAAGG 3′. The mutation on putative ARE3 was incorporated into the reverse primer as described above. Luciferase reporter assays were performed following the manufacturer's protocol. Briefly, the reporter vectors or control pGL-3 vector together with a Renilla luciferase vector were cotransfected into NRF2-expressing or control HEK293T cells as indicated. After 24 hours of incubation, the luciferase activity was determined using a Dual Luciferase Assay (Promega). The activity of firefly luciferase reporter was normalized by that of Renilla luciferase of each sample.

Mice and in vivo studies

PANC-1 or MIA Paca-2 cells stably expressing GFP under a cytomegalovirus (CMV) promoter were infected with lentiviral vectors expressing G6PD shRNA, G6PD cDNA, or the respective control. Cells were selected with puromycin (Invitrogen). Cells (0.5 million) were injected into each of the athymic nude mice (NCr nu/nu, male and female, 6 weeks old) via tail vein (*74*). After 8 weeks, the mice were euthanized and characterized for tumor formation in the lung and liver. Specifically, livers and lungs were dissected and imaged by an Olympus MVX10 fluorescent stereoscope (Olympus, Center Valley, PA) for GFP expression. One-third of the lung from each mouse was lysed with 1 ml of RIPA buffer after cryogenic homogenization with liquid nitrogen and mortar. The lysates of the lung were then analyzed by Western blot for GFP expression. Both human and mouse GAPDH proteins were used as a loading control. Two-thirds of the lung from each mouse was fixed with 4% PFA and embedded for tissue slides. Six livers of each group were randomly selected, fixed with 4% PFA, and embedded for tissue slides. A slide was made every 10 to 12 sections apart to cover more information on tumor formation in the lung and liver. Five slides of each block were processed for H&E staining for quantification of the number of tumor nodules and tumor areas by ImageJ Pro plus 7 software (Media Cybernetics). The average number of tumor nodules and the average size of total tumor areas of each H&E staining slide represent the tumor burden of the organ for each mouse. Slides of lung tissue from mice injected with control or G6PD-knockdown PANC-1 cells via tail vein were also assayed for G6PD expression by IHC staining. The antibody staining intensity of relatively large and small tumor nodules in the lung was quantified with Imagescope software (Aperio Technologies Inc.).

For the total NADP(H) pool quantification, 1 million GFP-labeled PANC-1 cells carrying lentiviral G6PD expression or control vector were injected into each athymic nude mouse (NCr nu/nu, male and female, 6 weeks old) via tail vein. A week later, 5 million (*75*) G6PD-overexpressing or control PANC-1 cells were subcutaneously injected into the flank of each athymic nude mouse that was already inoculated with G6PD-overexpressing or control PANC-1 cells via tail vein, respectively. After 10 weeks, the mice were euthanized and characterized for xenograft tumor and lung metastases. Specifically, each xenograft tumor was dissected, measured, and preserved (a small portion, ~50 mm^3) in liquid nitrogen immediately. Meanwhile, lungs of the mice were dissected and imaged by an Olympus MVX10 fluorescent stereoscope (Olympus, Center Valley, PA). One-half of the lung from each mouse was further dissected under a fluorescent stereoscope to only collect tumor cells with GFP. The collected tumor cells with GFP (~30 mm^3) were preserved in liquid nitrogen immediately. These preserved xenograft tumors and tumors dissected from the lung were lysed with buffer after cryogenic homogenization with liquid nitrogen and mortar. The total cellular $NADP^+$ and NADPH levels were determined by an NADP/NADPH quantitation colorimetric assay kit with an NADPH standard (BioVision Inc., San Francisco, CA) and normalized by the total protein of each sample. The remaining one-half of the lung from each mouse was fixed with 4% PFA, embedded for tissue slides, stained with H&E, and quantified for tumor areas to determine the tumor burden of the organ for each mouse as mentioned above.

The mice were housed at 20° to 22°C on a 12-hour light/dark cycle. The health status of the mice was closely monitored by behavior and body weights (twice a week) following the general Guide for the Care and Use of Laboratory Animals. All experiments involving animals were approved by the University of Pennsylvania Institutional Animal Care and Use Committee.

IHC staining of TMA

Formalin-fixed paraffin-embedded pancreatic cancer TMA slides, which included 29 primary tumors and 17 nodal or distant metastases, were acquired from the Cooperative Human Tissue Network (Mid-Atlantic Division). These TMA slides were stained for the expression of NRF2, PIRH2, E2F1, p73, G6PD, and NADK1 with respective antibodies. Briefly, these TMA slides were subjected to antigen retrieval using Novocastra Epitope Retrieval Solutions (pH 6) (Leica Biosystems, Wetzlar, Germany), followed by incubation with primary antibodies at 4°C overnight. Dako Dual Endogenous Enzyme Block (DAKO, Denmark) was used to neutralize endogenous peroxidase. The slides were then washed and incubated with biotinylated secondary antibody and linked to avidin with the VECTASTAIN ABC Kit (Vector Laboratories, Burlingame, CA). The antibody staining was developed with 3,3'-diaminobenzidine (DAB). In each tumor sample (each section in the array), at least six randomly chosen cancer areas were captured at ×40 magnification. The antibody staining intensity of each tumor sample was quantified with Imagescope software (Aperio Technologies Inc.). The attributed [arbitrary units (a.u.)] antibody staining intensity for each tumor sample was calculated by dividing the highest antibody staining intensity of a tumor sample in the TMA slide and transformed by multiplying by 10.

Analysis of patient samples

mRNA levels (a.u.) of G6PD and PIRH2 in pancreatic primary tumors and metastases were extracted from the Gene Expression Omnibus dataset (GSE63124). mRNA levels of NRF2, p73, and G6PD (in reads per kilobase million) in patients with pancreatic cancer were extracted from the Human Protein Atlas (www.proteinatlas.org/) (*76*) for Pearson's correlation and coefficient analysis. The survival data of pancreatic cancer patients with high or low of NRF2, PIRH2, E2F1, p73, G6PD, and NADK1 expression were extracted from the Human Protein Atlas (www.proteinatlas.org/) (*76*) and analyzed for survival probability with the parameters indicated in table S1.

Data analysis

The heatmap was performed using the online algorithm, following the manual's instructions (https://software.broadinstitute.org/morpheus/). Statistical analyses were performed using two-way analysis of variance (ANOVA) or Student's *t* test of GraphPad Prism 8. No other methods were used to determine whether the data met the assumptions of the statistical approach or not. Detailed statistics can also be found in the figures and figure legends.

SUPPLEMENTARY MATERIALS

Supplementary material for this article is available at https://science.org/doi/10.1126/sciadv.abo0404

View/request a protocol for this paper from *Bio-protocol*.

REFERENCES AND NOTES

1. T. Finkel, Signal transduction by reactive oxygen species. *J. Cell Biol.* **194**, 7–15 (2011).
2. L. A. Sena, N. S. Chandel, Physiological roles of mitochondrial reactive oxygen species. *Mol. Cell* **48**, 158–167 (2012).
3. H. Sies, C. Berndt, D. P. Jones, Oxidative stress. *Annu. Rev. Biochem.* **86**, 715–748 (2017).
4. D. Trachootham, J. Alexandre, P. Huang, Targeting cancer cells by ROS-mediated mechanisms: A radical therapeutic approach? *Nat. Rev. Drug Discov.* **8**, 579–591 (2009).
5. C. Gorrini, I. S. Harris, T. W. Mak, Modulation of oxidative stress as an anticancer strategy. *Nat. Rev. Drug Discov.* **12**, 931–947 (2013).
6. J. D. Hayes, A. T. Dinkova-Kostova, K. D. Tew, Oxidative stress in cancer. *Cancer Cell* **38**, 167–197 (2020).
7. Z. T. Schafer, A. R. Grassian, L. Song, Z. Jiang, Z. Gerhart-Hines, H. Y. Irie, S. Gao, P. Puigserver, J. S. Brugge, Antioxidant and oncogene rescue of metabolic defects caused by loss of matrix attachment. *Nature* **461**, 109–113 (2009).
8. S. Vanharanta, J. Massague, Origins of metastatic traits. *Cancer Cell* **24**, 410–421 (2013).
9. V. I. Sayin, M. X. Ibrahim, E. Larsson, J. A. Nilsson, P. Lindahl, M. O. Bergo, Antioxidants accelerate lung cancer progression in mice. *Sci. Transl. Med.* **6**, 221ra15 (2014).
10. E. Piskounova, M. Agathocleous, M. M. Murphy, Z. Hu, S. E. Huddlestun, Z. Zhao, A. M. Leitch, T. M. Johnson, R. J. DeBerardinis, S. J. Morrison, Oxidative stress inhibits distant metastasis by human melanoma cells. *Nature* **527**, 186–191 (2015).
11. K. Le Gal, M. X. Ibrahim, C. Wiel, V. I. Sayin, M. K. Akula, C. Karlsson, M. G. Dalin, L. M. Akyürek, P. Lindahl, J. Nilsson, M. O. Bergo, Antioxidants can increase melanoma metastasis in mice. *Sci. Transl. Med.* **7**, 308re8 (2015).
12. C. Wiel, K. L. Gal, M. X. Ibrahim, C. A. Jahangir, M. Kashif, H. Yao, D. V. Ziegler, X. Xu, T. Ghosh, T. Mondal, C. Kanduri, P. Lindahl, V. I. Sayin, M. O. Bergo, BACH1 stabilization by antioxidants stimulates lung cancer metastasis. *Cell* **178**, 330–345.e22 (2019).
13. M. Breau, A. Houssaini, L. Lipskaia, S. Abid, E. Born, E. Marcos, G. Czibik, A. Attwe, D. Beaulieu, A. Palazzo, J. M. Flaman, B. Bourachot, G. Collin, J. T. van Nhieu, D. Bernard, F. Mechta-Grigoriou, S. Adnot, The antioxidant N-acetylcysteine protects from lung emphysema but induces lung adenocarcinoma in mice. *JCI Insight* **4**, e127647 (2019).
14. Y. Zhang, Y. Xu, W. Lu, J. M. Ghergurovich, L. Guo, I. A. Blair, J. D. Rabinowitz, X. Yang, Upregulation of antioxidant capacity and nucleotide precursor availability suffices for oncogenic transformation. *Cell Metab.* **33**, 94–109.e8 (2021).
15. L. Jiang, A. A. Shestov, P. Swain, C. Yang, S. J. Parker, Q. A. Wang, L. S. Terada, N. D. Adams, M. T. McCabe, B. Pietrak, S. Schmidt, C. M. Metallo, B. P. Dranka, B. Schwartz, R. J. DeBerardinis, Reductive carboxylation supports redox homeostasis during anchorage-independent growth. *Nature* **532**, 255–258 (2016).
16. O. G. McDonald, X. Li, T. Saunders, R. Tryggvadottir, S. J. Mentch, M. O. Warmoes, A. E. Word, A. Carrer, T. H. Salz, S. Natsume, K. M. Stauffer, A. Makohon-Moore, Y. Zhong, H. Wu, K. E. Wellen, J. W. Locasale, C. A. Iacobuzio-Donahue, A. P. Feinberg, Epigenomic reprogramming during pancreatic cancer progression links anabolic glucose metabolism to distant metastasis. *Nat. Genet.* **49**, 367–376 (2017).
17. A. Tasdogan, B. Faubert, V. Ramesh, J. M. Ubellacker, B. Shen, A. Solmonson, M. M. Murphy, Z. Gu, W. Gu, M. Martin, S. Y. Kasitinon, T. Vandergriff, T. P. Mathews, Z. Zhao, D. Schadendorf, R. J. DeBerardinis, S. J. Morrison, Metabolic heterogeneity confers differences in melanoma metastatic potential. *Nature* **577**, 115–120 (2020).
18. C. G. Miller, A. Holmgren, E. S. J. Arner, E. E. Schmidt, NADPH-dependent and -independent disulfide reductase systems. *Free Radic. Biol. Med.* **127**, 248–261 (2018).
19. W. Ying, NAD^+/NADH and $NADP^+$/NADPH in cellular functions and cell death: Regulation and biological consequences. *Antioxid. Redox Signal.* **10**, 179–206 (2008).
20. N. Pollak, C. Dolle, M. Ziegler, The power to reduce: Pyridine nucleotides—Small molecules with a multitude of functions. *Biochem. J.* **402**, 205–218 (2007).
21. L. Chen, Z. Zhang, A. Hoshino, H. D. Zheng, M. Morley, Z. Arany, J. D. Rabinowitz, NADPH production by the oxidative pentose-phosphate pathway supports folate metabolism. *Nat. Metab.* **1**, 404–415 (2019).
22. P. Jiang, W. Du, A. Mancuso, K. E. Wellen, X. Yang, Reciprocal regulation of p53 and malic enzymes modulates metabolism and senescence. *Nature* **493**, 689–693 (2013).
23. J. Fan, J. Ye, J. J. Kamphorst, T. Shlomi, C. B. Thompson, J. D. Rabinowitz, Quantitative flux analysis reveals folate-dependent NADPH production. *Nature* **510**, 298–302 (2014).
24. A. Stincone, A. Prigione, T. Cramer, M. M. C. Wamelink, K. Campbell, E. Cheung, V. Olin-Sandoval, N. M. Grüning, A. Krüger, M. Tauqeer Alam, M. A. Keller, M. Breitenbach, K. M. Brindle, J. D. Rabinowitz, M. Ralser, The return of metabolism: Biochemistry and physiology of the pentose phosphate pathway. *Biol. Rev. Camb. Philos. Soc.* **90**, 927–963 (2015).
25. Z. Zhang, L. Chen, L. Liu, X. Su, J. D. Rabinowitz, Chemical basis for deuterium labeling of fat and NADPH. *J. Am. Chem. Soc.* **139**, 14368–14371 (2017).
26. C. Cosentino, D. Grieco, V. Costanzo, ATM activates the pentose phosphate pathway promoting anti-oxidant defence and DNA repair. *EMBO J.* **30**, 546–555 (2011).
27. A. Kuehne, H. Emmert, J. Soehle, M. Winnefeld, F. Fischer, H. Wenck, S. Gallinat, L. Terstegen, R. Lucius, J. Hildebrand, N. Zamboni, Acute activation of oxidative pentose phosphate pathway as first-line response to oxidative stress in human skin cells. *Mol. Cell* **59**, 359–371 (2015).
28. H. L. Zhou, R. Zhang, P. Anand, C. T. Stomberski, Z. Qian, A. Hausladen, L. Wang, E. P. Rhee, S. M. Parikh, S. A. Karumanchi, J. S. Stamler, Metabolic reprogramming by the S-nitroso-CoA reductase system protects against kidney injury. *Nature* **565**, 96–100 (2019).
29. D. Anastasiou, G. Poulogiannis, J. M. Asara, M. B. Boxer, J. K. Jiang, M. Shen, G. Bellinger, A. T. Sasaki, J. W. Locasale, D. S. Auld, C. J. Thomas, M. G. Vander Heiden, L. C. Cantley, Inhibition of pyruvate kinase M2 by reactive oxygen species contributes to cellular antioxidant responses. *Science* **334**, 1278–1283 (2011).
30. P. Jiang, W. du, X. Wang, A. Mancuso, X. Gao, M. Wu, X. Yang, p53 regulates biosynthesis through direct inactivation of glucose-6-phosphate dehydrogenase. *Nat. Cell Biol.* **13**, 310–316 (2011).
31. M. B. Sporn, K. T. Liby, NRF2 and cancer: The good, the bad and the importance of context. *Nat. Rev. Cancer* **12**, 564–571 (2012).
32. Y. Mitsuishi, K. Taguchi, Y. Kawatani, T. Shibata, T. Nukiwa, H. Aburatani, M. Yamamoto, H. Motohashi, Nrf2 redirects glucose and glutamine into anabolic pathways in metabolic reprogramming. *Cancer Cell* **22**, 66–79 (2012).
33. L. V. Eggleston, H. A. Krebs, Regulation of the pentose phosphate cycle. *Biochem. J.* **138**, 425–435 (1974).
34. C. Riganti, E. Gazzano, M. Polimeni, E. Aldieri, D. Ghigo, The pentose phosphate pathway: An antioxidant defense and a crossroad in tumor cell fate. *Free Radic. Biol. Med.* **53**, 421–436 (2012).
35. G. Hoxhaj, I. Ben-Sahra, S. E. Lockwood, R. C. Timson, V. Byles, G. T. Henning, P. Gao, L. M. Selfors, J. M. Asara, B. D. Manning, Direct stimulation of NADP(+) synthesis through Akt-mediated phosphorylation of NAD kinase. *Science* **363**, 1088–1092 (2019).
36. T. Schild, M. R. McReynolds, C. Shea, V. Low, B. E. Schaffer, J. M. Asara, E. Piskounova, N. Dephoure, J. D. Rabinowitz, A. P. Gomes, J. Blenis, NADK is activated by oncogenic signaling to sustain pancreatic ductal adenocarcinoma. *Cell Rep.* **35**, 109238 (2021).
37. R. L. Siegel, K. D. Miller, H. E. Fuchs, A. Jemal, Cancer statistics, 2021. *CA Cancer J. Clin.* **71**, 7–33 (2021).
38. J. D. Mizrahi, R. Surana, J. W. Valle, R. T. Shroff, Pancreatic cancer. *Lancet* **395**, 2008–2020 (2020).
39. L. Liu, X. Su, W. J. Quinn III, S. Hui, K. Krukenberg, D. W. Frederick, P. Redpath, L. Zhan, K. Chellappa, E. White, M. Migaud, T. J. Mitchison, J. A. Baur, J. D. Rabinowitz, Quantitative analysis of NAD synthesis-breakdown fluxes. *Cell Metab.* **27**, 1067–1080.e5 (2018).
40. J. M. Ghergurovich, J. C. G.-Cañaveras, J. Wang, E. Schmidt, Z. Zhang, T. TeSlaa, H. Patel, L. Chen, E. C. Britt, M. P.-Nebot, M. C. Gomez-Cabrera, A. Lahoz, J. Fan, U. H. Beier, H. Kim, J. D. Rabinowitz, A small molecule G6PD inhibitor reveals immune dependence on pentose phosphate pathway. *Nat. Chem. Biol.* **16**, 731–739 (2020).
41. W. Du, W. Du, P. Jiang, A. Mancuso, A. Stonestrom, M. D. Brewer, A. J. Minn, T. W. Mak, M. Wu, X. Yang, TAp73 enhances the pentose phosphate pathway and supports cell proliferation. *Nat. Cell Biol.* **15**, 991–1000 (2013).

42. P. Jiang, W. Du, X. Yang, A critical role of glucose-6-phosphate dehydrogenase in TAp73-mediated cell proliferation. *Cell Cycle* **12**, 3720–3726 (2013).
43. M. Biswas, J. Y. Chan, Role of Nrf1 in antioxidant response element-mediated gene expression and beyond. *Toxicol. Appl. Pharmacol.* **244**, 16–20 (2010).
44. A. Oberst, M. Rossi, P. Salomoni, P. P. Pandolfi, M. Oren, G. Melino, F. Bernassola, Regulation of the p73 protein stability and degradation. *Biochem. Biophys. Res. Commun.* **331**, 707–712 (2005).
45. M. Rossi, V. D. Laurenzi, E. Munarriz, D. R. Green, Y. C. Liu, K. H. Vousden, G. Cesareni, G. Melino, The ubiquitin-protein ligase Itch regulates p73 stability. *EMBO J.* **24**, 836–848 (2005).
46. Y. S. Jung, Y. Qian, X. Chen, The p73 tumor suppressor is targeted by Pirh2 RING finger E3 ubiquitin ligase for the proteasome-dependent degradation. *J. Biol. Chem.* **286**, 35388–35395 (2011).
47. L. Gonzalez-Cano, A. L. Hillje, S. Fuertes-Alvarez, M. M. Marques, A. Blanch, R. W. Ian, M. S. Irwin, J. C. Schwamborn, M. C. Marín, Regulatory feedback loop between TP73 and TRIM32. *Cell Death Dis.* **4**, e704 (2013).
48. M. Urist, T. Tanaka, M. V. Poyurovsky, C. Prives, p73 induction after DNA damage is regulated by checkpoint kinases Chk1 and Chk2. *Genes Dev.* **18**, 3041–3054 (2004).
49. V. H. Freedman, S. I. Shin, Cellular tumorigenicity in nude mice: Correlation with cell growth in semi-solid medium. *Cell* **3**, 355–359 (1974).
50. L. N. Kent, G. Leone, The broken cycle: E2F dysfunction in cancer. *Nat. Rev. Cancer* **19**, 326–338 (2019).
51. E. L. Deer, J. González-Hernández, J. D. Coursen, J. E. Shea, J. Ngatia, C. L. Scaife, M. A. Firpo, S. J. Mulvihill, Phenotype and genotype of pancreatic cancer cell lines. *Pancreas* **39**, 425–435 (2010).
52. D. Melisi, J. Niu, Z. Chang, Q. Xia, B. Peng, S. Ishiyama, D. B. Evans, P. J. Chiao, Secreted interleukin-1α induces a metastatic phenotype in pancreatic cancer by sustaining a constitutive activation of nuclear factor-κB. *Mol. Cancer Res.* **7**, 624–633 (2009).
53. N. Pollak, M. Niere, M. Ziegler, NAD kinase levels control the NADPH concentration in human cells. *J. Biol. Chem.* **282**, 33562–33571 (2007).
54. Y. H. Tsang, T. Dogruluk, P. M. Tedeschi, J. Wardwell-Ozgo, H. Lu, M. Espitia, N. Nair, R. Minelli, Z. Chong, F. Chen, Q. E. Chang, J. B. Dennison, A. Dogruluk, M. Li, H. Ying, J. R. Bertino, M. C. Gingras, M. Ittmann, J. Kerrigan, K. Chen, C. J. Creighton, K. Eterovic, G. B. Mills, K. L. Scott, Functional annotation of rare gene aberration drivers of pancreatic cancer. *Nat. Commun.* **7**, 10500 (2016).
55. D. H. Tran, R. Kesavan, H. Rion, M. H. Soflaee, A. Solmonson, D. Bezwada, H. S. Vu, F. Cai, J. A. Phillips III, R. J. DeBerardinis, G. Hoxhaj, Mitochondrial $NADP^+$ is essential for proline biosynthesis during cell growth. *Nat. Metab.* **3**, 571–585 (2021).
56. J. Zhu, S. Schwörer, M. Berisa, Y. J. Kyung, K. W. Ryu, J. Yi, X. Jiang, J. R. Cross, C. B. Thompson, Mitochondrial NADP(H) generation is essential for proline biosynthesis. *Science* **372**, 968–972 (2021).
57. W. Kuo, J. Lin, T. K. Tang, Human glucose-6-phosphate dehydrogenase (G6PD) gene transforms NIH 3T3 cells and induces tumors in nude mice. *Int. J. Cancer* **85**, 857–864 (2000).
58. J. M. Ghergurovich, M. Esposito, Z. Chen, J. Z. Wang, V. Bhatt, T. Lan, E. White, Y. Kang, J. Y. Guo, J. D. Rabinowitz, Glucose-6-phosphate dehydrogenase is not essential for K-Ras-driven tumor growth or metastasis. *Cancer Res.* **80**, 3820–3829 (2020).
59. G. Melino, V. De Laurenzi, K. H. Vousden, p73: Friend or foe in tumorigenesis. *Nat. Rev. Cancer* **2**, 605–615 (2002).
60. U. M. Moll, N. Slade, p63 and p73: Roles in development and tumor formation. *Mol. Cancer Res.* **2**, 371–386 (2004).
61. L. Li, L. Li, W. Li, T. Chen, Bin Zou, L. Zhao, H. Wang, X. Wang, L. Xu, X. Liu, D. Wang, B. Li, T. W. Mak, W. du, X. Yang, P. Jiang, TAp73-induced phosphofructokinase-1 transcription promotes the Warburg effect and enhances cell proliferation. *Nat. Commun.* **9**, 4683 (2018).
62. H. Ding, Z. Chen, K. Wu, S. M. Huang, W. Wu, S. E. LeBoeuf, R. G. Pillai, J. D. Rabinowitz, T. Papagiannakopoulos, Activation of the NRF2 antioxidant program sensitizes tumors to G6PD inhibition. *Sci. Adv.* **7**, eabk1023 (2021).
63. J. Bartkova, Z. Hořejší, K. Koed, A. Krämer, F. Tort, K. Zieger, P. Guldberg, M. Sehested, J. M. Nesland, C. Lukas, T. Ørntoft, J. Lukas, J. Bartek, DNA damage response as a candidate anti-cancer barrier in early human tumorigenesis. *Nature* **434**, 864–870 (2005).
64. V. G. Gorgoulis, L. V. F. Vassiliou, P. Karakaidos, P. Zacharatos, A. Kotsinas, T. Liloglou, M. Venere, R. A. DiTullio Jr., N. G. Kastrinakis, B. Levy, D. Kletsas, A. Yoneta, M. Herlyn, C. Kittas, T. D. Halazonetis, Activation of the DNA damage checkpoint and genomic instability in human precancerous lesions. *Nature* **434**, 907–913 (2005).
65. E. Blanchet, J. S. Annicotte, S. Lagarrigue, V. Aguilar, C. Clapé, C. Chavey, V. Fritz, F. Casas, F. Apparailly, J. Auwerx, L. Fajas, E2F transcription factor-1 regulates oxidative metabolism. *Nat. Cell Biol.* **13**, 1146–1152 (2011).
66. J. D. Graves, Y. J. Lee, K. Liu, G. Li, F. T. Lin, W. C. Lin, E2F1 sumoylation as a protective cellular mechanism in oxidative stress response. *Proc. Natl. Acad. Sci. U.S.A.* **117**, 14958–14969 (2020).
67. M. Irwin, M. C. Marin, A. C. Phillips, R. S. Seelan, D. I. Smith, W. Liu, E. R. Flores, K. Y. Tsai, T. Jacks, K. H. Vousden, W. G. Kaelin Jr., Role for the p53 homologue p73 in E2F-1-induced apoptosis. *Nature* **407**, 645–648 (2000).
68. W. N. Tian, L. D. Braunstein, J. Pang, K. M. Stuhlmeier, Q. C. Xi, X. Tian, R. C. Stanton, Importance of glucose-6-phosphate dehydrogenase activity for cell growth. *J. Biol. Chem.* **273**, 10609–10617 (1998).
69. G. Rey, U. K. Valekunja, K. A. Feeney, L. Wulund, N. B. Milev, A. Stangherlin, L. Ansel-Bollepalli, V. Velagapudi, J. S. O'Neill, A. B. Reddy, The pentose phosphate pathway regulates the circadian clock. *Cell Metab.* **24**, 462–473 (2016).
70. A. J. Covarrubias, R. Perrone, A. Grozio, E. Verdin, NAD^+ metabolism and its roles in cellular processes during ageing. *Nat. Rev. Mol. Cell Biol.* **22**, 119–141 (2021).
71. S. Hui, J. M. Ghergurovich, R. J. Morscher, C. Jang, X. Teng, W. Lu, L. A. Esparza, T. Reya, le Zhan, J. Y. Guo, E. White, J. D. Rabinowitz, Glucose feeds the TCA cycle via circulating lactate. *Nature* **551**, 115–118 (2017).
72. W. Lu, L. Wang, L. Chen, S. Hui, J. D. Rabinowitz, Extraction and quantitation of nicotinamide adenine dinucleotide redox cofactors. *Antioxid. Redox Signal.* **28**, 167–179 (2018).
73. M. F. Clasquin, E. Melamud, J. D. Rabinowitz, LC-MS data processing with MAVEN: A metabolomic analysis and visualization engine. *Curr. Protoc. Bioinformatics* **Chapter 14**, Unit14.11 (2012).
74. A. Nagarajan, S. K. Dogra, L. Sun, N. Gandotra, T. Ho, G. Cai, G. Cline, P. Kumar, R. A. Cowles, N. Wajapeyee, Paraoxonase 2 facilitates pancreatic cancer growth and metastasis by stimulating GLUT1-mediated glucose transport. *Mol. Cell* **67**, 685–701.e6 (2017).
75. A. Y. Yong, Y. A. Yu, C. Galanis, Y. Woo, N. Chen, Q. Zhang, Y. Fong, A. A. Szalay, Regression of human pancreatic tumor xenografts in mice after a single systemic injection of recombinant vaccinia virus GLV-1h68. *Mol. Cancer Ther.* **8**, 141–151 (2009).
76. M. Uhlen, C. Zhang, S. Lee, E. Sjöstedt, L. Fagerberg, G. Bidkhori, R. Benfeitas, M. Arif, Z. Liu, F. Edfors, K. Sanli, K. von Feilitzen, P. Oksvold, E. Lundberg, S. Hober, P. Nilsson, J. Mattsson, J. M. Schwenk, H. Brunnström, B. Glimelius, T. Sjöblom, P.-H. Edqvist, D. Djureinovic, P. Micke, C. Lindskog, A. Mardinoglu, F. Ponten, A pathology atlas of the human cancer transcriptome. *Science* **357**, eaan2507 (2017).

Acknowledgments: We thank CHTN for providing TMA of pancreatic cancer; Penn Molecular Pathology and Imaging Core for processing mouse tissues and H&E staining; G. Zhu, S. Ghaisas, H. Wu, X. He, N. Zhou, Z. Cheng, and Y. Liang for technical assistance. **Funding:** This study was supported by grants from NIH (R01CA182675, R01CA184867, R01CA235760, R01CA243520, R50CA211437, and 5T32CA115299). **Author contributions:** X.Y. and Y.Z. conceived the project and designed the experiments. X.Y. and E.J.B. supervised the project. Y.Z. performed most experiments. Y.X. performed ChIP assay and helped with other experiments. J.L. and B.Z.S. advised and helped with metastasis experiments. S.Y. performed some cell culture experiments and helped with the animal study. W.L. performed and J.D.R. supervised the metabolic profiling and the flux of $NADP^+$ de novo biosynthesis analysis. X.Y. and Y.Z. analyzed the data and wrote the manuscript. All other authors commented on the manuscript. **Competing interests:** J.D.R. is a paid consultant of Pfizer; a founder, director, and stockholder of Farber Partners; a founder and stockholder in Toran Therapeutics; inventor of patents in the area of G6PD and NADPH metabolism held by Princeton University; and a director of the Princeton University-PKU Shenzhen collaboration. The other authors declare that they have no competing interests. **Data and materials availability:** All data needed to evaluate the conclusions in the paper are present in the paper and/or the Supplementary Materials.

Submitted 10 January 2022
Accepted 3 June 2022
Published 20 July 2022
10.1126/sciadv.abo0404